The Astrophysical Journal, 841:37 (19pp), 2017 May 20 https://doi.org/10.3847/1538-4357/aa6f16

Hints on the Gradual Resizing of the Torus in AGNs through Decomposition of *Spitzer*/IRS Spectra

Omaira González-Martín[1], Josefa Masegosa[2], Antonio Hernán-Caballero[3], Isabel Márquez[2], Cristina Ramos Almeida[4,5], Almudena Alonso-Herrero[6,7], Itziar Aretxaga[8], José Miguel Rodríguez-Espinosa[4,5], Jose Antonio Acosta-Pulido[4,5], Lorena Hernández-García[9], Donaji Esparza-Arredondo[1], Mariela Martínez-Paredes[1], Paolo Bonfini[1], Alice Pasetto[1], and Deborah Dultzin[1]

[1] Instituto de Radioastronomía y Astrofísica (IRyA-UNAM), 3-72 (Xangari), 8701, Morelia, Mexico; o.gonzalez@crya.unam.mx
[2] Instituto de Astrofísica de Andalucía, CSIC, Glorieta de la Astronomía s/n E-18008, Granada, Spain
[3] Departamento de Astrofísica, Facultad de CC. Físicas, Universidad Complutense de Madrid, E-28040 Madrid, Spain
[4] Instituto de Astrofísica de Canarias (IAC), C/Vía Láctea, s/n, E-38205 La Laguna, Spain
[5] Departamento de Astrofísica, Universidad de La Laguna (ULL), E-38205 La Laguna, Spain
[6] Centro de Astrobiología (CAB, CSIC-INTA), ESAC Campus, E-28692 Villanueva de la Cañada, Madrid, Spain
[7] Visiting Professor, Department of Physics and Astronomy, University of Texas at San Antonio, TX 78249, USA
[8] Instituto Nacional de Astrofísica, Óptica y Electrónica (INAOE), Luis Enrique Erro 1, Sta. Ma. C.P. 72840 Tonantzintla, Puebla, Mexico
[9] INAF—Istituto di Astrofisica e Planetologia Spaziali di Roma (IAPS), Via del Fosso del Cavaliere 100, I-00133 Roma, Italy
Received 2017 February 16; revised 2017 March 29; accepted 2017 April 18; published 2017 May 22

Abstract

Several authors have claimed that less luminous active galactic nuclei (AGNs) are not capable of sustaining a dusty torus structure. Thus, a gradual resizing of the torus is expected when the AGN luminosity decreases. Our aim is to examine mid-infrared observations of local AGNs of different luminosities for the gradual resizing and disappearance of the torus. We applied the decomposition method described by Hernán-Caballero et al. to a sample of ∼100 *Spitzer*/IRS spectra of low-luminosity AGNs and powerful Seyferts in order to decontaminate the torus component from other contributors. We have also included Starburst objects to ensure secure decomposition of the *Spitzer*/IRS spectra. We have used the affinity propagation (AP) method to cluster the data into five groups within the sample according to torus contribution to the 5–15 μm range ($C_{\rm torus}$) and bolometric luminosity ($L_{\rm bol}$). The AP groups show a progressively higher torus contribution and an increase of the bolometric luminosity from Group 1 ($C_{\rm torus} \sim 0\%$ and $\log(L_{\rm bol}) \sim 41$) up to Group 5 ($C_{\rm torus} \sim 80\%$ and $\log(L_{\rm bol}) \sim 44$). We have fitted the average spectra of each of the AP groups to clumpy models. The torus is no longer present in Group 1, supporting its disappearance at low luminosities. We were able to fit the average spectra for the torus component in Groups 3 ($C_{\rm torus} \sim 40\%$ and $\log(L_{\rm bol}) \sim 42.6$), 4 ($C_{\rm torus} \sim 60\%$ and $\log(L_{\rm bol}) \sim 43.7$), and 5 to Clumpy torus models. We did not find a good fitting to Clumpy torus models for Group 2 ($C_{\rm torus} \sim 18\%$ and $\log(L_{\rm bol}) \sim 42$). This might suggest a different configuration and/or composition of the clouds for Group 2, which is consistent with the different gas content seen in Groups 1, 2, and 3, according to detections of H_2 molecular lines. Groups 3, 4, and 5 show a trend of decreasing torus width (which leads to a likely decrease of the geometrical covering factor), although we cannot confirm it with the present data. Finally, Groups 3, 4, and 5 show an increase of the outer radius of the torus for higher luminosities, consistent with a resizing of the torus according to AGN luminosity.

Key words: galaxies: active – galaxies: nuclei – infrared: galaxies

Supporting material: figure set, machine-readable tables

1. Introduction

According to the unification of active galactic nuclei (AGNs), the central engine is surrounded by a dusty, optically thick structure responsible for partially blocking its view (the so-called dusty torus). The AGN is powered by a supermassive black hole (SMBH) that is fed by its accretion disk. Low- and high-velocity clouds are located at the narrow- and broad-line regions (NLR and BLR, respectively), the latter being located inside the dusty structure. Much of the observed diversity of AGN families is simply explained as the result of the line of sight toward this asymmetric torus structure. Reviews on the unification schemes for AGNs have been presented by Antonucci (1993) and Urry & Padovani (1995). There are still open questions on the nature and geometry of the torus that need to be settled (see e.g., Netzer 2015 and references therein).

It was realized quite early that the nuclear dust could be distributed in clumps (Krolik & Begelman 1988). AGN tori have a range of properties (e.g., width, size, composition, number of clouds, distribution of clouds, etc.), where the covering factor is also a key parameter to classify the object as a type-1 or type-2 AGN (Alonso-Herrero et al. 2011; Ramos Almeida et al. 2011; Elitzur 2012; Mateos et al. 2016). Although there is considerable observational support for the unified model, some observations and AGN classes have casted doubt on the most extreme form of the unified model, in which the viewing angle is the only parameter responsible for the AGN classification. For instance, Ricci et al. (2011) showed that the X-ray reflection component (associated with the torus) was intrinsically stronger for type-2 than for type-1 AGNs. Ramos Almeida et al. (2011) found that type-2 AGNs have tori with larger covering factors than type-1 AGNs using clumpy torus models. Mendoza-Castrejón et al. (2015 and references therein) have shown that the structure of the torus might even depend on the nearby environment of the host galaxy. An example of an AGN family that is not easy to explain with AGN ingredients are; low-ionization nuclear emission-line

regions (LINERs; Heckman 1980). Their spectral energy distribution (SED) is clearly different from those of other AGN (Ho 2008; Mason et al. 2013).

Using mass conservation arguments, Elitzur & Shlosman (2006) showed that the dusty torus cannot be sustained under certain AGN bolometric luminosities, claiming the torus disappears. Hönig & Beckert (2007) studied the balance between gravity and radiation pressure from the central source for the torus, and found that the torus changes its characteristics and obscuration, becoming insufficient for luminosities of the order of $\sim 10^{42}$ erg s^{-1}. Elitzur & Ho (2009) showed that indeed this limit on the AGN bolometric luminosity depends on the SMBH mass. Recently, Elitzur & Netzer (2016) realized that besides this luminosity limit, there is a range on the bolometric luminosities in which the torus still might disappear depending on the combination of some of the parameters of the wind. From an observational point of view, the lack of an infrared bump in low-luminosity AGNs (LLAGNs), which is associated with dust obscuration in other AGNs, provides evidence for unobscured nuclei (Ho 2008). UV variability also gives rise to an unobstructed view of the accretion disk (Maoz et al. 2005; Hernández-García et al. 2014, 2016).

Very little has been said about the dependence of the size of the torus (i.e., outer radius of the torus) on the AGN luminosity. Mason et al. (2013) already suggested a different torus from that in Seyferts, in light of their low dust-to-gas ratio, although a large diversity of contributions were also found. Müller-Sánchez et al. (2013) showed evidence in favor of the gradual disappearance of the torus, finding that the molecular gas in some LINERs is almost 10 times more concentrated toward the center and with column densities $\sim$3 times smaller than in Seyfert galaxies. Indeed, González-Martín et al. (2015) showed that a large fraction of LLAGNs with 2–10 keV X-ray luminosities $L_X < 10^{41}$ erg s^{-1} may lack torus signatures at mid-infrared. Although they excluded objects with a large contamination of the ISM, these results might be somehow contaminated by the host galaxies due to the low spatial resolution inherent to the *Spitzer* data they used (Alonso-Herrero et al. 2006; Sturm et al. 2006; Mason et al. 2013). Indeed, the nuclear emission of LLAGNs is affected by the host galaxy contribution, even at X-rays (González-Martín et al. 2014).

Here we take advantage of the spectral decomposition method developed by Hernán-Caballero et al. (2015, hereafter HC15) to isolate the AGN component, and analyze the disappearance of the torus in the same sample used by González-Martín et al. (2015). Furthermore, a full analysis of AGNs with a wide range of bolometric luminosities (more than six orders of magnitude) also allows us to test the gradual disappearance of the torus.

The paper is organized as follows. In Section 2 we describe the sample. The data are presented in Section 3 and the analysis is presented in Section 4. In Section 5 we analyze the torus contribution at mid-infrared (i.e., the torus contribution since mid-infrared is fully dominated by the torus) as a function of the bolometric luminosity of the AGN. A full discussion of the results is presented in Section 6. Throughout this paper we use the Hubble constant $H_0 = 70$ km s^{-1} Mpc^{-1}.

2. Sample

The sample was originally presented by González-Martín et al. (2015). The LINER sample is selected as those objects with reported X-ray luminosities from González-Martín et al. (2009a) with full coverage of the 5–30 μm range with the InfraRed Spectrograph (*Spitzer*/IRS) spectra. This guarantees that all of the LINERs have $L_X(2\text{–}10\,keV)$ measurements. Among the 48 LINERs with *Spitzer*/IRS spectra, 40 mid-infrared spectra were taken from the CASSIS atlas (Lebouteiller et al. 2011) and 8 from the SINGS database (Kennicutt et al. 2003). The main properties of the LINER sample are presented in Table 1, where we split the sample into type-1 (all of them Type 1.9) and type-2 LINERs according to the optical classification done by Véron-Cetty & Véron (2010) and Ho et al. (1997).

It is well known that the LINER classification, based only on the preponderance of low-ionization emission lines at optical wavelengths, yields a mixture of different types of objects (Ho 2008 and references therein). Our sample is based on available X-ray observations. Hence, it could be biased toward an AGN nature since these observations might have been done because of the known AGN component in these sources. Indeed, 90% of the X-ray sample was classified as AGN dominated based on multiwavelength evidences such as the existence of a point-like source at hard X-rays (28 out of the 48 LINERs), the presence of iron Kα emission lines at 6.4 keV (26 out of the 48 LINERs), radio compact sources or radio-jet detections (31 out of the 48 LINERs), UV variability (5 out of the 48 sources), and broad Hα emission lines (8 out of the 48 LINERs). We refer the reader to Tables 11 and 12 in González-Martín et al. (2009a) for further details. Adding all these evidence together, among the 48 LINERs selected for the present analysis, only two sources lack evidence of an AGN (UGC 4881 and NGC 4676A), consistent with the idea that our sample contains AGN-like LINERs.

For consistency with our previous work, the Seyfert and Starburst samples are the same as those studied in González-Martín et al. (2015). The Seyfert sample contains all the type-1 and type-2 sources included in Shi et al. (2006), the Compton-thick sample described by Goulding et al. (2012), and the SINGS sample. In total, it contains 42 Seyferts. Among them, 32 are type-2 Seyferts (S2, including 20 Compton-thick and 12 Compton-thin) and 10 are type-1 Seyferts (S1). The Starburst sample has been taken from Ranalli et al. (2003), Brandl et al. (2006), and Grier et al. (2011). This Starburst sample contains 19 sources. The main properties of Seyferts and Starbursts are included in Tables 2 and 3, respectively.

Thus, our final sample includes 48 LINERs, 42 Seyferts, and 19 Starburst (109 objects). We have compared the absolute *B* magnitude and velocity distributions for local AGNs from the Palomar sample (Ho et al. 2003 and references therein) with the sample analyzed here. We found that our LINER, Seyfert, and Starburst samples have the same distributions as local AGNs. Thus, although this is not a complete sample, it is representative of the population of nearby AGNs.

In order to avoid further bias in our results, we have investigated whether the physical angular resolution we obtain from *Spitzer*/IRS spectra depends on the class of the object. We have computed the inner portion of the galaxy (in parsec units) according to the slit width of the IRS spectra (slit width of 3.6 arcsec) at the distance of each object. This portion of galaxy extending out from the nucleus is recorded as "slit width" in Col. 5 of Tables 1–3. The median "slit width" of the sample is 520 pc, with 25th–75th percentiles of [340–1170] pc. The "slit width" distribution according to their optical class is

Table 1
Details of the LINER Sample and Results of *Spitzer*/IRS Decomposition

Object name (1)	Type (2)	D (Mpc) (3)	$\log(L_X)$ (4)	Slit width (pc) (5)	$C_{\rm torus}$ (%) (6)	$C_{\rm Stellar}$ (%) (7)	$C_{\rm ISM}$ (%) (8)	RMSE (9)	AP (10)
NGC 315	LINER1	56.0	41.8	1159	$39.8^{+3.6}_{-2.7}$	$22.3^{+8.8}_{-4.5}$	$36.4^{+4.6}_{-8.7}$	0.071	3
NGC 1052	LINER1	19.7	41.5	408	$76.2^{+3.9}_{-2.9}$	$15.4^{+5.0}_{-5.1}$	$7.2^{+4.2}_{-3.8}$	0.056	5
NGC 1097	LINER1	19.6	40.8	406	$0.6^{+1.3}_{-0.6}$	$5.6^{+4.0}_{-2.8}$	$92.4^{+3.0}_{-3.8}$	0.049	1
NGC 2639	LINER1	47.7	40.3	986	$11.6^{+4.6}_{-4.7}$	43^{+21}_{-23}	44^{+24}_{-22}	0.178	2
NGC 4438	LINER1	13.4	39.0	282	$0.6^{+1.3}_{-0.6}$	$26.0^{+2.9}_{-6.1}$	$71.9^{+5.9}_{-2.8}$	0.13	1
NGC 4450♣	LINER1	16.1	40.3	333	$0.0^{+0.7}_{-0.0}$	66^{+24}_{-4}	33^{+4}_{-24}	0.48	1
NGC 4579	LINER1	19.6	41.2	402	$14.1^{+2.3}_{-4.0}$	63^{+10}_{-15}	21^{+14}_{-10}	0.101	2
NGC 5005	LINER1	20.6	39.9	426	$1.3^{+1.6}_{-1.3}$	23^{+10}_{-15}	75^{+14}_{-10}	0.104	1
III Zw 035	LINER2	117.5	40.0	2431	$0.4^{+1.1}_{-0.4}$	$0.0^{+0.7}_{-0.0}$	$98.6^{+0.9}_{-1.1}$	0.818	1
NGC 835	LINER2	34.0	41.4	703	$2.6^{+3.1}_{-2.4}$	$11.0^{+9.0}_{-7.3}$	$85.7^{+7.2}_{-9.0}$	0.091	1
NGC 1291♣	LINER2	8.6	39.0	178	$0.7^{+1.5}_{-0.7}$	$73.1^{+6.2}_{-6.6}$	$25.3^{+5.8}_{-5.9}$	0.106	1
NGC 2685♣	LINER2	13.3	39.0	274	$6.6^{+5.5}_{-5.1}$	68^{+18}_{-16}	25^{+12}_{-15}	0.104	1
NGC 2655	LINER2	24.4	41.2	505	$18.5^{+2.5}_{-2.8}$	53^{+13}_{-19}	26^{+21}_{-13}	0.077	2
UGC 04881	LINER2	168.3	38.4	3482	$0.0^{+0.7}_{-0.0}$	$1.7^{+2.3}_{-1.7}$	$97.3^{+1.7}_{-2.3}$	0.053	1
3C 218	LINER2	235.0	42.1	4862	33^{+19}_{-20}	31^{+28}_{-22}	48^{+27}_{-30}	0.177	3
NGC 2841♣	LINER2	17.3	39.2	358	$0.8^{+1.7}_{-0.8}$	$72.9^{+8.7}_{-9.2}$	$25.5^{+9.0}_{-8.4}$	0.167	1
UGC 05101	LINER2	168.6	42.1	3488	$11.0^{+3.3}_{-6.2}$	$5.3^{+5.2}_{-4.3}$	$83.1^{+6.4}_{-7.4}$	0.08	2
NGC 3079	LINER2	19.3	42.1	399	$25.2^{+7.5}_{-7.4}$	$2.4^{+2.5}_{-2.4}$	$74.8^{+4.4}_{-8.2}$	0.122	2
NGC 3185	LINER2	22.9	39.4	473	$1.2^{+1.7}_{-1.2}$	19 ± 12	78 ± 12	0.082	1
NGC 3190	LINER2	24.3	39.5	504	$0.2^{+1.1}_{-0.2}$	$26.7^{+8.0}_{-7.5}$	$70.9^{+8.3}_{-8.5}$	0.086	1
NGC 3627	LINER2	9.8	39.4	202	$0.6^{+1.3}_{-0.6}$	$26.7^{+7.2}_{-7.3}$	$71.7^{+7.5}_{-5.3}$	0.064	1
NGC 3628	LINER2	10.9	39.9	225	$12.2^{+1.3}_{-4.9}$	$2.0^{+1.3}_{-1.3}$	$84.2^{+2.0}_{-1.4}$	0.172	2
NGC 4125♣	LINER2	22.0	38.7	455	$0.1^{+1.1}_{-0.1}$	$88.0^{+7.1}_{-7.0}$	$10.8^{+6.9}_{-7.3}$	0.322	1
IRAS 12112+0305	LINER2	314.0	41.2	6496	$1.2^{+1.2}_{-1.1}$	$0.0^{+0.7}_{-0.0}$	$97.8^{+1.1}_{-1.2}$	0.758	1
NGC 4261	LINER2	29.9	41.0	619	$26.3^{+2.6}_{-3.3}$	$48.1^{+7.1}_{-9.8}$	23^{+8}_{-10}	0.098	2
NGC 4321♣	LINER2	16.4	40.5	340	$9.3^{+7.0}_{-6.2}$	51 ± 10	37^{+6}_{-11}	0.116	1
NGC 4374♣	LINER2	16.7	39.5	346	$2.7^{+2.6}_{-2.5}$	78 ± 11	17.0 ± 10	0.07	1
NGC 4486	LINER2	16.7	40.7	344	15^{+9}_{-10}	66^{+19}_{-21}	19^{+18}_{-14}	0.099	2
NGC 4552♣	LINER2	16.0	39.2	330	$0.1^{+1.1}_{-0.1}$	$97.9^{+1.4}_{-1.6}$	$1.1^{+1.6}_{-1.1}$	0.216	1
NGC 4589♣	LINER2	28.1	38.9	581	$0.6^{+1.3}_{-0.6}$	76^{+14}_{-13}	26^{+10}_{-16}	0.109	1
NGC 4594♣	LINER2	11.1	39.9	230	$0.1^{+1.1}_{-0.1}$	$85.0^{+5.6}_{-5.6}$	$13.5^{+5.6}_{-5.6}$	0.075	1
NGC 4676A	LINER2	94.5	39.9	1955	$0.0^{+1.0}_{-0.0}$	$2.2^{+4.6}_{-2.2}$	$96.6^{+2.4}_{-2.8}$	0.075	1
NGC 4698♣	LINER2	23.3	38.7	469	$1.5^{+1.9}_{-1.5}$	77^{+14}_{-16}	21^{+15}_{-14}	0.122	1
NGC 4696♣	LINER2	37.6	40.0	778	$4.7^{+4.3}_{-4.0}$	$84.9^{+9.4}_{-8.6}$	$11.9^{+7.6}_{-8.4}$	0.166	1
NGC 4736♣	LINER2	5.1	38.6	105	$0.0^{+0.8}_{-0.0}$	51^{+8}_{-15}	47^{+15}_{-8}	0.115	1
MRK 266SW	LINER2	118.2	42.2	2446	32^{+9}_{-17}	9^{+11}_{-7}	60^{+17}_{-15}	0.059	3
MRK 266NE	LINER2	120.1	41.6	2485	$11.7^{+6.6}_{-6.9}$	$7.4^{+8.4}_{-6.0}$	81^{+10}_{-11}	0.083	2
UGC 08696	LINER2	161.8	43.0	3348	$45.5^{+1.2}_{-1.2}$	$0.0^{+0.7}_{-0.0}$	$53.5^{+1.2}_{-1.2}$	0.129	3
IRAS 14348-1447	LINER2	355.5	41.7	7354	$7.4^{+1.2}_{-1.3}$	$0.0^{+0.7}_{-0.0}$	$91.6^{+1.3}_{-1.2}$	0.851	1
NGC 5866	LINER2	12.2	38.3	253	$0.0^{+0.7}_{-0.0}$	29^{+29}_{-5}	70^{+5}_{-29}	0.096	1
NGC 6251	LINER2	98.2	42.8	2032	$35.8^{+1.8}_{-1.6}$	46^{+10}_{-15}	18^{+15}_{-9}	0.149	3
NGC 6240	LINER2	104.8	42.4	2169	$20.2^{+2.5}_{-1.7}$	$0.0^{+0.7}_{-0.0}$	$78.8^{+1.7}_{-2.5}$	0.081	2
IRAS 17208-0014	LINER2	183.3	41.2	3793	$0.7^{+1.2}_{-0.7}$	$0.0^{+0.7}_{-0.0}$	$98.3^{+0.8}_{-1.2}$	1.075	1
NGC 7130	LINER2	69.2	42.9	1431	43^{+17}_{-16}	$2.7^{+3.2}_{-2.5}$	54^{+18}_{-15}	0.032	3
NGC 7331	LINER2	14.2	40.5	295	$4.5^{+3.2}_{-3.5}$	41^{+9}_{-11}	$52.8^{+9.9}_{-7.5}$	0.071	1
IC 1459	LINER2	24.0	40.5	497	19 ± 10	63^{+11}_{-15}	$14.6^{+8.4}_{-7.5}$	0.083	2
NPM1G-12.0625	LINER2	23.3	41.5	469	25^{+18}_{-17}	40 ± 28	48^{+34}_{-33}	0.69	2
NGC 7743	LINER2	21.1	39.5	438	$4.3^{+3.6}_{-3.5}$	43^{+15}_{-21}	50^{+22}_{-15}	0.105	1

Note. AP: Affinity Propagation groups (1 to 5, see the text). X-ray luminosity given in units of erg s^{-1}. ♣: Candidates lacking a torus because they belong to Group 1 with $C_{\rm ISM} < 50\%$ (see the text).

(This table is available in machine-readable form.)

shown in Figure 1. Although there is an apparent lack of Starbursts with larger "slit widths" while type-1 Seyferts tend to show larger "slit widths," according to a K-S test we cannot reject the possibility that all optical classes come from the same parent distribution. Thus, biases due to the distance of the objects can be ruled out.

Table 2
Details of the Comparison Samples and Results of *Spitzer*/IRS Decomposition

Object Name (1)	Type (2)	D (Mpc) (3)	$\log(L_X)$ (4)	Slit Width (pc) (5)	C_{torus} (%) (6)	$C_{Stellar}$ (%) (7)	C_{ISM} (%) (8)	RMSE (9)	AP (10)
MCG-6-30-15	S1	33.2	42.8	687	79 ± 14	17^{+15}_{-12}	$9.4^{+8.6}_{-6.7}$	0.031	5
Fairall9	S1	201.4	44.0	4166	$87.5^{+3.1}_{-5.1}$	$4.1^{+3.7}_{-3.4}$	$6.7^{+5.0}_{-4.1}$	0.034	5
NGC 526A	S1	81.8	43.2	1692	$82.6^{+8.5}_{-8.5}$	$13.2^{+9.4}_{-7.8}$	$4.8^{+4.8}_{-3.9}$	0.06	5
NGC 3783	S1	47.8	42.8	988	$69.5^{+8.8}_{-8.4}$	21^{+11}_{-14}	$9.5^{+9.6}_{-7.3}$	0.038	4
IC 4329A	S1	68.8	43.7	1422	79^{+12}_{-9}	$15.4^{+6.4}_{-7.7}$	$5.6^{+5.4}_{-4.4}$	0.034	5
NGC 5548	S1	216.8	42.8	4484	$64.3^{+4.7}_{-3.0}$	$16.7^{+8.1}_{-7.4}$	$16.4^{+8.6}_{-8.1}$	0.081	4
H1846-786	S1	317.4	44.6	6567	76^{+16}_{-17}	$11.6^{+9.7}_{-8.6}$	16^{+13}_{-12}	0.055	5
MRK 509	S1	240.5	44.1	4976	$72.1^{+6.0}_{-6.8}$	$11.3^{+5.3}_{-6.5}$	$14.0^{+6.7}_{-4.9}$	0.039	5
NGC 7213	S1	22.0	42.2	455	$71.8^{+2.8}_{-4.6}$	$14.9^{+8.9}_{-7.7}$	$12.7^{+8.0}_{-6.5}$	0.099	5
MCG-2-58-22	S1	200.7	44.3	4152	82 ± 11	14 ± 10	$8.8^{+8.6}_{-6.8}$	0.028	5
MRK 1066	S2	51.7	42.9	1070	38^{+16}_{-12}	$4.1^{+3.6}_{-3.4}$	57^{+13}_{-15}	0.036	3
NGC 1386	S2	16.1	41.6	334	55^{+8}_{-13}	13^{+8}_{-10}	$36.1^{+6.8}_{-9.6}$	0.089	4
NGC 2110	S2	35.6	42.4	736	71^{+10}_{-12}	19^{+15}_{-14}	$13.0^{+7.5}_{-8.5}$	0.053	4
ESO 005-G004	S2	25.6	41.9	531	$25.3^{+7.3}_{-3.4}$	16^{+15}_{-9}	57^{+11}_{-16}	0.117	2
MRK 3	S2	63.2	44.4	1308	$86.4^{+4.5}_{-2.0}$	$0.2^{+3.3}_{-0.2}$	$12.0^{+2.5}_{-7.0}$	0.093	5
NGC 2273	S2	31.0	42.2	641	57^{+14}_{-15}	14^{+13}_{-10}	33^{+13}_{-14}	0.03	4
IRAS 07145-2914	S2	23.2	42.5	480	83^{+11}_{-9}	$5.4^{+6.4}_{-4.4}$	$14.0^{+8.2}_{-8.9}$	0.075	5
MCG-5-23-16	S2	36.3	43.0	752	$80.1^{+7.7}_{-7.3}$	$12.4^{+8.9}_{-9.1}$	$9.8^{+7.8}_{-5.9}$	0.027	5
NGC 3081	S2	26.5	42.5	548	$62.4^{+5.1}_{-3.4}$	$11.6^{+4.9}_{-6.8}$	$25.9^{+5.7}_{-4.4}$	0.106	4
NGC 3281	S2	45.7	43.2	946	78^{+12}_{-21}	$10.9^{+15.4}_{-8.1}$	16^{+14}_{-9}	0.058	5
NGC 3393	S2	53.6	42.9	1108	$58.8^{+1.8}_{-3.4}$	$4.4^{+2.3}_{-2.9}$	$36.3^{+9.1}_{-3.6}$	0.314	4
NGC 3621	S2	6.9	39.3	142	$1.2^{+1.5}_{-1.2}$	$21.8^{+2.2}_{-6.4}$	$75.1^{+6.9}_{-1.8}$	0.156	1
NGC 4388	S2	20.5	42.5	417	58^{+14}_{-4}	$6.2^{+4.8}_{-3.3}$	36^{+7}_{-17}	0.131	4
NGC 4507	S2	50.5	43.1	1046	78^{+10}_{-11}	$13^{+11}_{-9.0}$	$11.2^{+7.5}_{-6.8}$	0.039	5
NGC 4725♣	S2	13.6	38.9	281	$0.0^{+0.7}_{-0.0}$	63^{+27}_{-2}	36^{+2}_{-26}	0.278	1
MRK 231	S2	180.6	44.3	3736	$44.2^{+6.4}_{-3.0}$	$0.2^{+1.2}_{-0.2}$	$50.8^{+6.3}_{-3.5}$	0.138	3
NGC 4941	S2	17.0	41.3	351	72^{+10}_{-12}	11^{+10}_{-8}	19^{+15}_{-13}	0.052	5
NGC 4939	S2	38.9	42.6	805	87^{+9}_{-13}	$6.8^{+8.5}_{-5.6}$	11^{+11}_{-9}	0.118	5
NGC 4945	S2	3.9	42.3	81	$0.9^{+1.7}_{-0.9}$	$0.0^{+0.7}_{-0.0}$	$98.1^{+0.9}_{-1.7}$	0.7	1
NGC 5135	S2	58.6	43.1	1213	$19.4^{+9.1}_{-9.8}$	$9.5^{+7.6}_{-7.0}$	$71.1^{+8.9}_{-8.5}$	0.028	2
NGC 5194	S2	8.0	40.9	165	$0.2^{+1.1}_{-0.2}$	$11.0^{+2.6}_{-2.9}$	$87.4^{+2.9}_{-2.7}$	0.059	1
NGC 5347	S2	27.3	42.4	565	$88.7^{+5.5}_{-7.3}$	$5.0^{+8.4}_{-4.2}$	$8.3^{+7.4}_{-6.2}$	0.054	5
Circinus Galaxy	S2	4.2	41.9	87	$43.8^{+6.3}_{-5.9}$	$7.3^{+4.5}_{-6.3}$	$48.8^{+5.9}_{-4.9}$	0.276	3
NGC 5506	S2	23.8	43.0	493	$66.3^{+8.3}_{-8.7}$	$19.7^{+9.7}_{-7.9}$	$11.0^{+6.3}_{-4.9}$	0.04	4
NGC 5643	S2	16.9	42.6	350	76^{+12}_{-8}	$1.4^{+4.7}_{-1.4}$	24^{+8}_{-12}	0.06	5
NGC 5728	S2	30.5	43.0	631	$23.1^{+9.4}_{-4.9}$	$10.7^{+9.4}_{-6.5}$	67^{+9}_{-12}	0.137	2
ESO 138-G001	S2	39.1	42.8	810	$46.2^{+5.2}_{-5.2}$	24^{+11}_{-10}	28^{+13}_{-16}	0.141	3
ESO 103-G035	S2	56.9	43.4	1177	74^{+11}_{-6}	$12.9^{+5.2}_{-10.3}$	$15.1^{+4.6}_{-4.9}$	0.085	5
IRAS 19254-7245	S2	264.3	44.5	5468	75 ± 13	$3.3^{+2.5}_{-2.4}$	20^{+13}_{-12}	0.031	5
NGC 7172	S2	33.9	42.7	701	43^{+5}_{-15}	9^{+12}_{-7}	49^{+8}_{-11}	0.145	3
NGC 7314	S2	18.2	42.3	376	81^{+12}_{-14}	12^{+11}_{-8}	14^{+12}_{-11}	0.076	5
NGC 7582	S2	21.2	42.6	439	38 ± 15	11^{+12}_{-9}	58^{+15}_{-16}	0.046	3

Note. AP: Affinity Propagation groups (1 to 5, see the text). X-ray luminosity given in units of erg s^{-1}. ♣: Candidates that do not have a torus because they belong to Group 1 with $C_{ISM} < 50\%$ (see the text).

(This table is available in machine-readable form.)

3. Data

3.1. Spitzer/IRS Spectra

We have only included spectra observed with both the short-low (SL) and long-low (LL) modules to guarantee the full *Spitzer*/IRS coverage (∼5–30 μm). CASSIS and SINGS provide flux- and wavelength-calibrated spectra. However, the observations using data from both the SL and LL spectral modules suffer from mismatches due to telescope pointing inaccuracies or due to different spatial resolutions of the IRS orders. This is not corrected in the final products given by CASSIS and SINGS. We therefore scaled each spectra to the immediate prior (in wavelength range) to overcome such effects. Thus, our flux level is scaled to the level of the shortest wavelengths, which is the order with the highest spatial resolution (3.6 arcsec). This guarantees that the flux level is scaled to the best spatial resolution that *Spitzer* can provide. Note, however, that this does not solve the problem related to the fact that each IRS module might be seeing a different region due to a different spatial resolution and/or slight changes on

Table 3
Details of the Comparison Samples and Results of *Spitzer*/IRS Decomposition

Object Name (1)	Type (2)	D (Mpc) (3)	$\log(L_X)$ (4)	Slit Width (pc) (5)	$C_{\rm torus}$ (%) (6)	$C_{\rm Stellar}$ (%) (7)	$C_{\rm ISM}$ (%) (8)	RMSE (9)	AP (10)
NGC 520	SB	34.4	40.0	712	$0.8^{+1.3}_{-0.8}$	$0.0^{+0.7}_{-0.0}$	$98.2^{+1.2}_{-1.3}$	0.085	1
NGC 0855	SB	9.3	37.9	192	$0.0^{+1.1}_{-0.0}$	23^{+27}_{-16}	76^{+16}_{-26}	0.133	1
NGC 0925	SB	8.6	38.3	178	$0.0^{+0.9}_{-0.0}$	25^{+25}_{-10}	74^{+10}_{-25}	0.456	1
IC 342	SB	3.4	39.0	69	$0.3^{+1.3}_{-0.3}$	$0.7^{+1.5}_{-0.7}$	$97.5^{+1.4}_{-1.5}$	0.07	1
NGC 1482	SB	19.6	39.4	405	$0.0^{+0.7}_{-0.0}$	$3.1^{+1.4}_{-1.3}$	$95.9^{+1.3}_{-1.4}$	0.061	1
NGC 1614	SB	68.3	41.3	1412	$0.4^{+1.3}_{-0.4}$	$1.2^{+2.3}_{-1.2}$	$97.3^{+1.8}_{-2.6}$	0.103	1
NGC 1808	SB	9.8	39.7	204	$0.1^{+1.1}_{-0.1}$	$1.4^{+2.0}_{-1.4}$	$97.2^{+1.8}_{-2.4}$	0.04	1
NGC 2146	SB	21.9	39.0	453	$0.0^{+0.7}_{-0.0}$	$1.6^{+2.1}_{-1.6}$	$97.7^{+1.8}_{-2.3}$	0.038	1
NGC 2798	SB	26.4	39.6	546	$0.0^{+0.7}_{-0.0}$	$7.0^{+2.4}_{-1.8}$	$92.2^{+1.7}_{-2.1}$	0.036	1
NGC 2903	SB	8.7	39.9	181	$1.9^{+2.4}_{-1.9}$	$5.6^{+5.7}_{-4.8}$	$92.5^{+5.1}_{-5.8}$	0.039	1
NGC 2976	SB	3.9	36.6	81	$0.0^{+0.7}_{-0.0}$	$20^{+12}_{-4.6}$	79^{+5}_{-12}	0.107	1
NGC 3184	SB	12.0	38.0	249	$0.0^{+1.0}_{-0.0}$	36^{+10}_{-20}	63^{+19}_{-10}	0.303	1
NGC 3198	SB	13.9	38.2	288	$0.0^{+0.7}_{-0.0}$	3^{+23}_{-3}	96^{+3}_{-23}	0.161	1
NGC 3256	SB	37.4	40.8	774	$0.1^{+1.1}_{-0.1}$	$2.1^{+1.6}_{-2.1}$	$96.2^{+2.4}_{-1.8}$	0.028	1
NGC 3310	SB	18.1	40.0	374	$2.3^{+1.5}_{-2.0}$	$0.0^{+0.7}_{-0.0}$	$96.7^{+2.0}_{-1.5}$	0.14	1
NGC 3367	SB	43.6	40.9	902	$6.0^{+3.4}_{-2.5}$	$0.0^{+0.7}_{-0.0}$	$93.0^{+2.5}_{-3.4}$	0.25	1
M108	SB	11.8	39.3	244	$1.2^{+1.6}_{-1.2}$	$8.6^{+5.9}_{-6.6}$	$88.6^{+7.5}_{-6.0}$	0.084	1
MRK 52	SB	33.5	38.0	693	$0.0^{+0.7}_{-0.0}$	$9.0^{+3.1}_{-2.4}$	$90.0^{+2.4}_{-3.1}$	0.193	1
NGC 7252	SB	58.6	40.6	1213	$1.3^{+2.1}_{-1.3}$	$5.2^{+6.7}_{-3.9}$	$93.7^{+3.6}_{-6.6}$	0.048	1

Note. AP: Affinity Propagation groups (1 to 5, see the text). X-ray luminosity given in units of erg s^{-1}. ♣:
(This table is available in machine-readable form.)

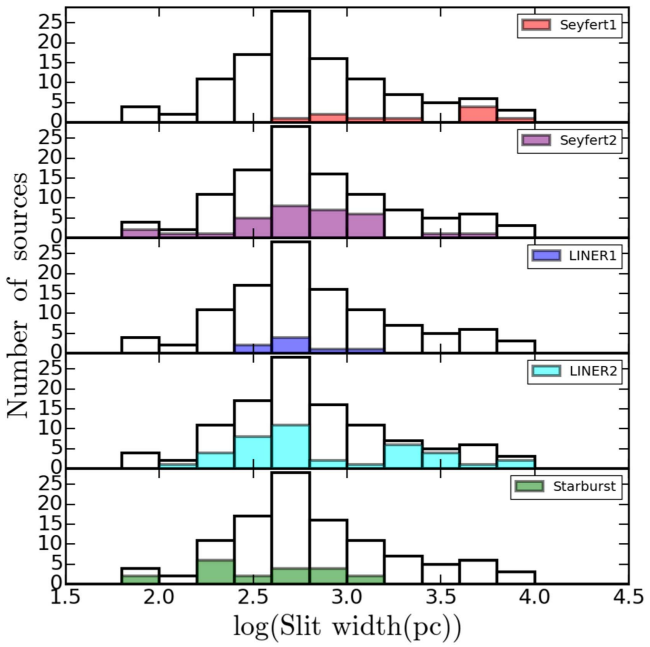

Figure 1. Distributions of "slit sizes" (in parsec) of the *Spitzer*/IRS spectra for the full sample (empty histograms in all panels) and for Seyfert 1 (red-filled histogram), Seyfert 2 (purple-filled histogram), LINER1 (cyan-filled histogram), LINER2 (blue-filled histogram), and Starbursts (green-filled histogram), from top to bottom.

the position of the spectrum. However, this is the best that we can do. Finally, the spectra are shifted to the rest frame according to the redshifts of the objects (see Col. 3 in Tables 1–3).

3.2. *CanariCam/GTC* 11.5 μm *Images*

We have included in our analysis mid-infrared spatially resolved images taken with CanariCam/GTC using the filter "Si6" centered at 11.5 μm. These observations are part of proprietary data of a sample of faint and Compton-thick LINERs observed with CanariCam/GTC (proposal ID GTC10-14A, P.I. González-Martín). Some of these images were already used by González-Martín et al. (2015) to compare their nuclear fluxes with *Spitzer*/IRS fluxes. Note that here we make a more sophisticated treatment of the images to better isolate the nuclear emission from its extended emission (see Section 4). The full sample contains 19 LINERs and it will be the subject of subsequent publications focused on the nuclear (J. Masegosa et al. 2017, in preparation; see Masegosa et al. 2013 for preliminary results on the nuclear flux) and extended emission (as an example, see the analysis of the extended emission of NGC 835 presented in González-Martín et al. 2016). Here we have used the nuclear flux taken from the CanariCam data in 12 objects in common with the *Spitzer*/IRS sample of LINERs. The summary of the observations used in this paper is reported in Table 4.

CanariCam uses a Raytheon 320 × 240 pixel Si:As detector that covers a field of view (FOV) of 26 × 19 arcsec on the sky with a pixel scale of 0.0798 arcsec. Standard mid-infrared chopping–nodding techniques were used to remove the time-variable sky background, the thermal emission from the telescope, and the detector $1/f$ noise. The employed chopping and nodding throws, and chop and nod position angles are reported in Table 4 (Col. 5).

Images of point-spread function (PSF) standard stars were obtained in the same filter immediately after the science target to accurately sample the image quality and allow for flux calibration of the target observations. Table 4 includes the

Table 4
CanariCam Observations

	Target Observations				Standard Star Observations				Results		
Name	Date (Y-M-D)	ObsID	Expt. (s)	Config.	Name (HD)	ObsID	Expt. (s)	$FWHM_{PSF}$ (arcsec)	$FWHM_N$ (arcsec)	$Flux_T$ (mJy)	$Flux_N$ (mJy)
(1)	(2)	(3)	(4)	(5)	(6)	(7)	(8)	(9)	(10)	(11)	(12)
NGC 315	2014 Sep 22	1048	927	10/10/90/-180	4502	1045	66	0.34-0.44	0.24–0.29	28 ± 5	9 ± 2
	2014 Sep 22	1050	927	10/10/90/-180	4502	1045	66	0.34–0.44			
NGC 835	2014 Sep 24	1281	993	10/10/90/-180	11353	1287	66	0.31–0.36	0.25-0.39	32 ± 5	27 ± 4
	2014 Sep 24	1283	993	10/10/90/-180	11353	1287	66	0.31–0.36			
NGC 2685*	2013 Jan 04	7636	661	10/10/90/-180	73108	7640	83	0.30–0.32	…	…	…
	2013 Jan 04	7638	661	10/10/90/-180	73108	7640	83	0.30–0.32			
NGC 2655	2013 Jan 04	7642	661	10/10/90/-180	73108	7640	83	0.30–0.32	0.26-0.27	29 ± 5	8 ± 1
	2013 Jan 04	7644	661	10/10/90/-180	73108	7640	83	0.30–0.32			
UGC 05101	2013 Jan 01	7270	617	10/10/90/-180	86378	7268	77	0.34–0.43	0.28-0.37	96 ± 15	11 ± 2
NGC 4321	2015 Apr-03	2700	927	10/10/90/-180	108381	2698	66	0.24–0.36	0.26-0.26	15 ± 3	3.0 ± 0.6
	2015 Apr-04	2702	927	10/10/90/-180	108381	2698	66	0.24–0.36			
NGC 4486	2015 Apr-06	3117	927	16/16/0/-180	108985	3113	66	0.36–0.42	0.28-0.33	14 ± 2	6 ± 1
	2015 Apr-06	3119	927	16/16/0/-180	108985	3113	66	0.36–0.42			
MRK 266NE	2013 Jan 01	7276	617	10/10/90/-180	120933	7272	77	0.32–0.35	0.37-0.46	34 ± 5	16 ± 3
MRK 266SW	2013 Jan 01	7276	617	10/10/90/-180	120933	7272	77	0.32–0.35	0.31-0.37	94 ± 15	11 ± 2
UGC 08696	2013 Jan 01	7274	308	10/10/90/-180	120933	7272	77	0.33–0.35	0.48-0.57	61 ± 10	25 ± 4
NGC 6251	2012 Sep 25	5990	617	12/12/0/-180	144204	5988	77	0.40–0.52	0.25-0.38	18 ± 3	7 ± 1
	2013 Aug 24	3063	662	16/16/0/0	144204	3061	66	0.25–0.26			
IRAS 17208-0014	2013 Jul 19	1897	596	10/10/90/-180	153210	1901	66	0.31–0.36	0.28-0.42	87 ± 14	4 ± 1
	2013 Jul 19	1899	596	10/10/90/-180	153210	1901	66	0.31–0.36			

Note. The object marked with an asterisk (NGC 2685) was not detected with CanariCam. The column called "Config." corresponds to the nod throw (keyword NODTHROW, in units of arcseconds), chop throw (keyword CHPTHROW, in units of arcseconds), instrument position angle (keyword INSTRPA, in degrees), and chop position angle (keyword CHPPA, in degrees; written as NODTHROW/CHPTHROW/INSTRPA/CHPPA).

name (Col. 6), integrating time (Col. 8), and the FWHM of the standard stars associated with each target (Col. 9, representing the FWHM of the PSF at the time of the observations). To compute it, we have fitted a 2D Gaussian to the standard star observations. The two numbers given in Col. 9 in Table 4 show the minor and major widths of this Gaussian fit. Any point-like source detected in our images should show an FWHM contained between these two values. However, as will be discussed below, the sky at mid-infrared is highly variable and often the conditions of the sky at the time the target was observed might have slightly changed from those when the standard star was observed. Thus, although this number can give a rough estimate of the image quality, it cannot be taken as a strict limit to the FWHM of a point-like source.

Each observing block was processed using the pipeline RedCan (González-Martín et al. 2013), which is able to produce flux-calibrated images and wavelength- and flux-calibrated spectra for CanariCam/GTC and T-ReCS/Gemini low-resolution data. The combination of the different observing blocks for the same source (when available; see Table 4) were made after flux calibration using Python routines.

3.3. Archival High Spatial Resolution Images

We have compiled all the high spatial resolution mid-infrared images associated with our *Spitzer*/IRS sample. For that purpose we have used the atlas of mid-infrared observations reported in Asmus et al. (2014). It contains 895 observations of 253 AGNs taken with 8 m class telescopes up to 2014.

This complements our study in three ways: (1) mid-infrared observations centered at wavelengths other than the 11.5 μm of the current CanariCam/GTC-observed LINERs, (2) mid-infrared observations of other LINERs not observed in our campaign with CanariCam/GTC, and (3) mid-infrared observations of objects included in our comparison samples. We have retrieved 285 mid-infrared observations for 18 LINERs, 10 type-1 Seyferts, 23 type-2 Seyferts, and two Starbursts contained in the atlas by Asmus et al. (2014). Among the LINERs, only five of them (UGC 05101, NGC 4486, MRK 266SW, MRK 266NE, and NGC 6251) are in common with the CanariCam/GTC sample, although not exactly with the same filter because the CanariCam/GTC sample was selected, avoiding objects already observed with 8 m class telescopes.

4. Analysis

4.1. Image Decomposition

Some of the high spatial resolution images in our sample show extended structures together with the nuclear point-like source (Asmus et al. 2015). In order to better isolate the nuclear component, we have developed a code able to decompose both emissions. This procedure is based on the idea that both emissions can be roughly fitted with 2D Gaussians. We have used a 2D Gaussian fit included in the package SATRAPY within Python, which allows the normalization of the Gaussian, the width along the major and minor axes, and the angle in which the major axis is located to be varied. First, we trim the image in a box of 40 × 40 pixels, centered at the position of the source, which is wide enough to contain all of the extended emission for all the objects in our sample but sufficiently small to guarantee that the procedure avoids any artificial or real structure away from our target. Then, we followed several steps

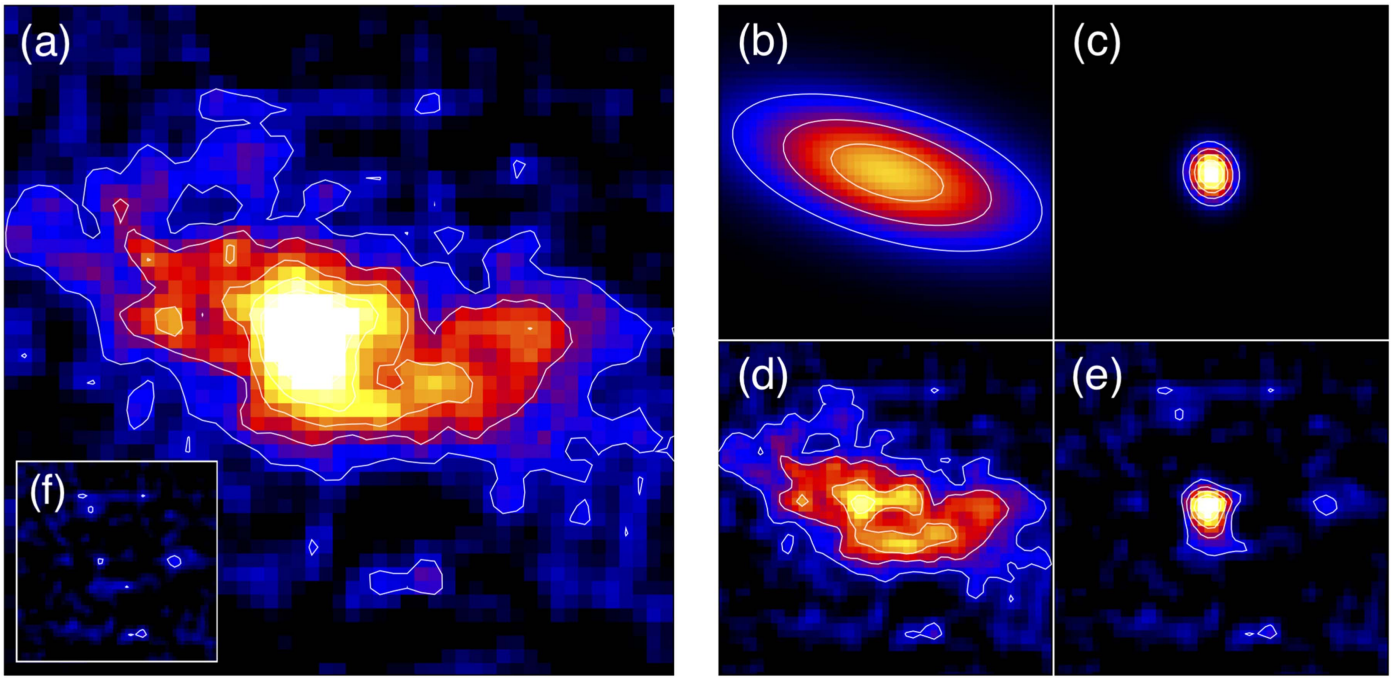

Figure 2. CanariCam 11.5 μm image of Mrk 266SW. The size of the inset box is 4 × 4 arcsec. East is up and north is right. (a) Total emission. (b) Gaussian model of the extended emission. (c) Gaussian model of the nuclear emission. (d) Extended emission after subtracting the nuclear emission model from the total emission (i.e., "a–c"). (e) Nuclear emission after subtracting the extended emission model from the total emission (i.e., "a–b"). (f, inset to panel (a)) Residuals after the fitting process (i.e., "a–b–c"). White contours show flux levels of 0.05, 0.1, 0.15, 0.2, and 0.25 mJy pixel^{-1}.

until the results converge to the final solution. (1) We fit the image using a single 2D Gaussian. At this stage, the width of the Gaussian is fixed to the width of the standard star associated with the target for CanariCam data (FWHM reported in Col. 9 of Table 4) or with the major axis of the FWHM of the Gaussian fit reported by Asmus et al. (2014). This is considered as an initial guess for the nuclear component. (2) The fitted Gaussian is subtracted from the original images, producing a first guess of the extended structure. This extended structure is fitted with another Gaussian, which is centered at the position of the first Gaussian but now allowing the widths of the Gaussian to vary. (3) This Gaussian fit to the extended emission is now subtracted from the original image, producing a new guess for the nuclear component. At this stage, the process starts over in (1), using this new guess for the nuclear component as the input image. This process continues until the residuals are within three standard deviations over the background of the image.

As an example of the result of this process, Figure 2 shows the case for Mrk 266SW. Panel (a) shows the original image where both point-like and extended emission can be clearly spotted. Panels (b) and (c) correspond to the best Gaussian fit to the extended and nuclear emissions, respectively. Panels (d) and (e) show the resulting "extended" and "nuclear" images, respectively, computed as the original image minus the Gaussian best fit for the nuclear component, and the original minus the Gaussian best fit for the extended emission. Panel (f) (inset in panel (a)) shows the residuals of the final fit. This method nicely isolates the nuclear from extended emission.

The resulting minor and major axes of the FWHM are recorded in Col. 10 in Table 4 for the CanariCam images and in Col. 3 in Table 5 for other archival data. In the case of CanariCam data, we can compare the final FHWM of the nuclear component with that of the PSF (as traced by the standard star). Although in most cases the FWHM of the nuclear component is consistent with that of the PSF, it is clear that in some cases the point-like source detected in the target image shows a smaller or larger FWHM than that of the standard star (e.g., UGC 08696 or NGC 315). When the FWHM of the nuclear component is larger than the PSF of the standard star, it is plausible that the source is partially resolved. However, it could also be due to changes on the

Table 5
Sample of Archival High-resolution Mid-IR Imaging Results

Name	Wavelength (μm)	FWHM$_N$ (arcsec)	Flux$_N$ (mJy)
NGC 1052	10.6	0.5-0.4	133 ± 24
	11.5	0.4–0.5	144 ± 26
	12.5	0.6–0.5	172 ± 31
	9.8	0.4–0.4	112 ± 20
	7.8	0.6–0.4	65 ± 11
	8.6	0.4–0.5	62 ± 11
	11.9	0.4–0.4	125 ± 21
	18.7	0.5–0.5	307 ± 51
	18.3	0.6–0.5	315 ± 53
	8.7	0.8–0.6	63 ± 10
NGC 1097	12.3	0.4–0.4	24.9 ± 4.2
	8.6	0.3–0.6	25.1 ± 4.2
	11.2	0.6–0.7	25.7 ± 4.5
	11.2	0.4–0.5	26.6 ± 4.4
	11.9	0.5–0.4	22.1 ± 3.9
	11.9	0.3–0.4	21.8 ± 3.7
	18.7	0.5–0.5	47.3 ± 7.9
	18.3	0.5–0.6	45.1 ± 7.7
	10.8	0.4–0.5	24.5 ± 4.1
	11.7	0.5–0.5	23.3 ± 4.0

(This table is available in its entirety in machine-readable form.)

conditions of the observation throughout the night. Due to the faintness of our targets, the exposure times are rather long. Thus, a delay of one hour or more between the observation of the target and that of the standard star is usual.

The nuclear fluxes (reported in Col. 11 of Table 4 and in Col. 4 of Table 5) are computed by performing aperture photometry in the nuclear images (i.e., after subtracting the extended emission), using an aperture radius 2.5 times the major width of the 2D Gaussian fit for the nuclear component. This ensures that over 97% of the flux is contained within this aperture and, at the same time, avoids any residuals of the extended emission contributing to the nuclear flux. We computed the error as the quadratic sum of the flux calibration uncertainty plus the error due to the S/N of each observation, but the errors are fully dominated by the former one. They are assumed to be 15% of the flux. Note that calibration errors need to be included especially when combining data sets from different facilities. Alonso-Herrero et al. (2016) computed the flux calibration in a sample of CanariCam/GTC observations of AGNs, finding that the mean calibration error is 11%, close to our estimate (see also Díaz-Santos et al. 2010; Ramos Almeida et al. 2011). We also compared the nuclear fluxes reported here with those reported by a Gaussian fit in Asmus et al. (2014). All of them are consistent within the errors. However, our errors are larger than those reported by Asmus et al. (2014). Note that our final purpose is to constrain the torus component when decomposing the *Spitzer*/IRS spectra. A less restrictive limit could translate into a larger contribution for this component. Since we are studying the plausible disappearance of the torus, this less restrictive constraint yields to a more conservative result on the disappearance of the torus (see Section 4.2).

4.2. Spectral Decomposition

We used the model-independent spectral decomposition called DeblendIRS presented by HC15 to decompose the *Spitzer*/IRS spectra. This code uses a set of IRS spectra as templates for purely stellar, interstellar (dominated by polycyclic aromatic hydrocarbons, PAHs), and AGN-dominated components. Here in after, we call these three components *stellar*, *ISM*, and *torus*, respectively. Note that we refer to the AGN component as the torus component since the torus is the dominant source of AGN continuum in the mid-infrared. The algorithm computes the marginalized probability distribution of physical parameters, from comparison of the observed data with all the models in the library, using Bayesian inference.

We initially have used as templates the same library presented by HC15. However, in their work, they focused on the decomposition in the range between 5 and 15 μm. For that reason, some of the templates did not cover the full *Spitzer*/IRS wavelength range. Our purpose is to decompose the full range covered by IRS spectra as much as possible in order to study the entire *Spitzer* spectra (and to compare with clumpy models). For that reason, we have removed the templates with redshift above 0.2. All together, we have removed 76 sources from the torus template list and 2 from the ISM list. This guarantees that all the templates can be used to decompose our local sample with spectra in the range 5.5–29 μm. We have chosen this range in order to maximize the number of templates that we are able to use, also maximizing the range covered. Finally, we have also removed from the AGN template library all the sources included in our current analysis (12 AGNs, mainly type-1 and type-2 Seyferts). The final template list contains 101 torus-, 59 ISM-, and 19 stellar-dominated spectra.

We have used the following constraints on the torus component to improve the uncertainty on the torus component as our aim is to study if the torus is present in our sample. First, we have used high spatial resolution data (described in Sections 3.2 and 3.3) to put an upper limit to the torus component flux at the specific observed wavelengths. Note that we are able to include these constraints because we know that the torus component is point like at both *Spitzer* and high-resolution imaging data. We used the flux measured in the nuclear component plus three times the error. Second, we have used the X-ray luminosity to set an upper limit to the torus component at 12 μm, using the well-established relation between the 12 μm and 2–10 keV X-ray luminosities for AGNs (Asmus et al. 2015). We have used the 12 μm to X-ray relation found by Asmus et al. (2015) because it is the most recent relation with the largest number of sources. Since X-ray luminosities can show short- and long-term variations, which can be as high as a factor of 10 (e.g., González-Martín & Vaughan 2012), we have assumed the error on the 2–10 keV X-ray luminosity to be a factor of 10. Then, we have used this value to estimate another upper limit to the 12 μm flux of the torus component. It is worth noticing that the X-ray to mid-infrared relation has been tested down to X-ray luminosities of L_X (2–10 keV) $\sim 10^{41}$ erg s^{-1} (Asmus et al. 2015). However, our current sample reaches X-ray luminosities down to L_X (2–10 keV) $\sim 10^{38}$ erg s^{-1}. Therefore, this relation might not apply to the very faint end of the luminosity function of AGNs. Indeed, one of the goals of this work is to test the plausible disappearance of the torus, although little is known of the very low-luminosity sources. In this case, we expect the 12 μm flux to be an upper limit to the actual contribution of the torus. Thus, using these limits as upper limits does not bias our results. Furthermore, this upper limit is very useful because it is available for all the objects in our sample.

We have used version 1.2 of the deblendIRS[11] code presented by HC15. It improves over previous versions in that it allows the flux priors to constrain the torus component to be included. For each object, we have decomposed its *Spitzer*/IRS spectrum, using the upper limit on the 12 μm flux (obtained from the 2–10 keV X-ray flux) and the mid-infrared fluxes obtained from high spatial resolution images. Figure 3 shows the best fit for the spectrum of the type-2 Seyfert galaxy NGC 5728 as an example.

Tables 1–3 include $C_{\rm torus}$ (Col. 6), $C_{\rm stellar}$ (Col. 7), and $C_{\rm ISM}$ (Col. 8) for the LINER, Seyfert, and Starburst samples, respectively. These values refer to the percentage of each component contributing to the 5–15 μm wavelength range. The Appendix shows the decomposition and posterior distributions for the full sample. The median values and 16th–84th percentiles for each class are listed in Table 6. Starbursts nicely group into $C_{\rm torus} < 1.3\%$, demonstrating the good performance of this method to decompose *Spitzer* spectra (see Table 6). Only NGC 3367 shows $C_{\rm torus} > 5\%$ (8.4%). This object might actually host an AGN (see González-Martín et al. 2015). Note that we have also confirmed that the change of the spectral range used for the decomposition to 5–15 μm has no impact in our results.

[11] http://www.denebola.org/ahc/deblendIRS

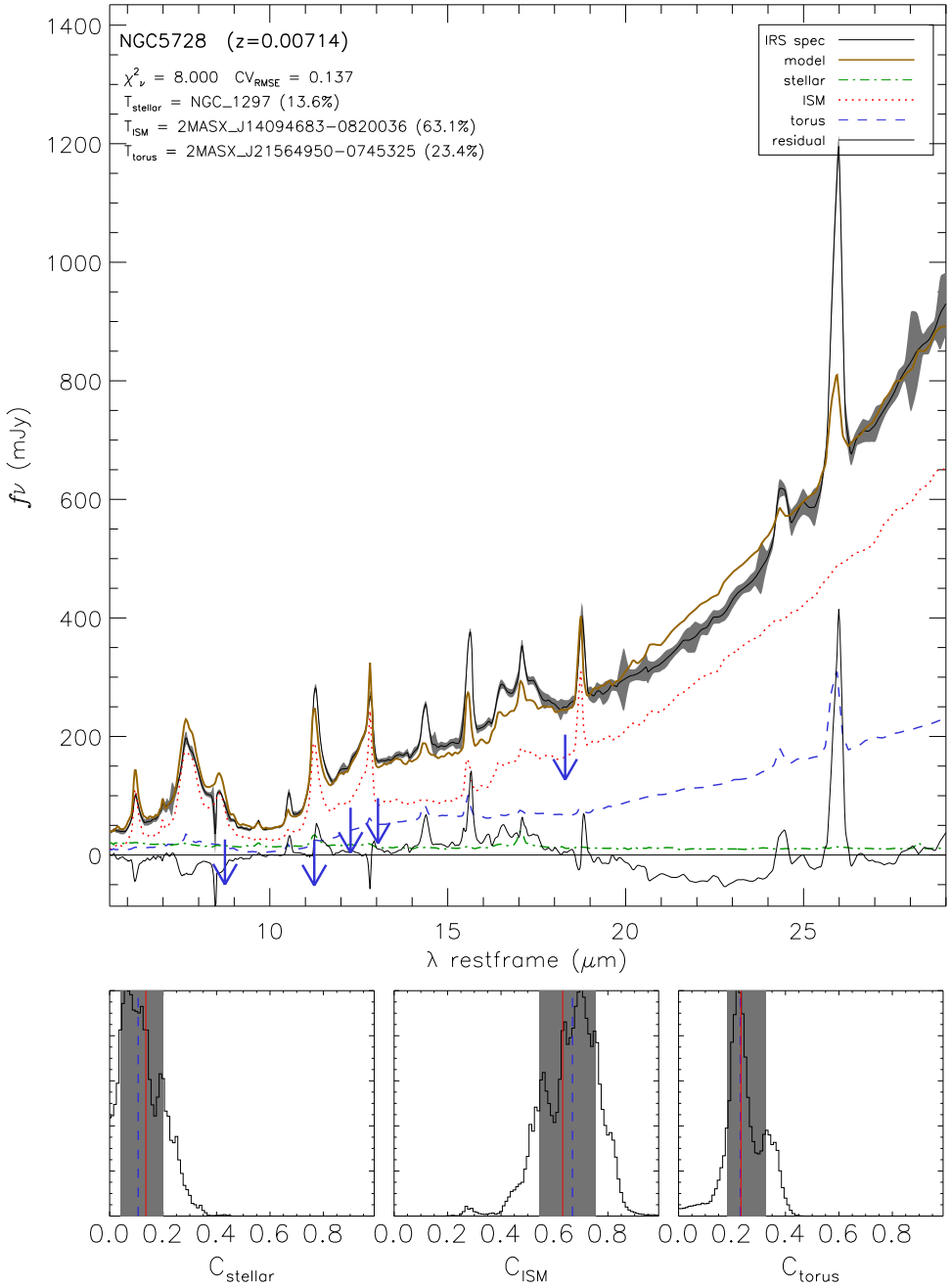

Figure 3. Best-fit decomposition models for the *Spitzer*/IRS spectrum of NGC 5728 (gray shaded area and the solid black line) using high-resolution data and X-ray luminosity as constraints for the decompositions (see the text). The (red) dotted, (blue) dashed, and (green) dotted–dashed lines represent the ISM, torus, and stellar components of the best-fitting model (shown by solid yellow line), respectively. The continuous line at the bottom of each plot shows the residuals (spectrum–model). Blue arrows (in the top panel) are the high-resolution data and 12 μm flux limit (derived from the X-ray luminosity) used as constraints for the final fit. The three bottom panels show $C_{stellar}$, C_{ISM}, and C_{torus} posterior distributions, from left to right.

Figure 4 shows a diagram representing the relative contribution of each component for the objects in our sample. Objects with 100% of a single component are located at one of the corners of this diagram (marked with their names in the diagram). Objects with 0% of one of the components would be located in the side of the triangle opposite to its corner. Interestingly, the diagram is not equally populated. There are no objects with $C_{ISM} \sim 0\%$, indicating that all the objects in our sample show a non-negligible ISM contribution. It is worth noting that each class can be clearly differentiated using their contributors. Starbursts are mainly dominated by ISM components. Type-1 Seyferts are fully dominated by the torus component with less than 30% of the stellar component, and with $C_{ISM} < 20\%$. Type-2 Seyferts have a wide range of torus and ISM components, with less than 30% of the stellar component. Finally, LINERs show less than 50% of the torus component with a wide range of both stellar and ISM components. The small number of type-1 LINERs prevents any firm conclusion on the difference between type-1 and type-2 LINERs to be reached.

The DeblendIRS code computes the root-mean-square error (RMSE) of the final fit for each object (included in Tables 1–3, Col. 9). We use these numbers to investigate when the final fit is good enough to represent the data. We have selected as bad fits

Table 6
Median and 16th and 84th Percentiles (in Parentheses) of the Torus, Stellar, and ISM Distributions

	C_{torus} (%)	$C_{stellar}$ (%)	C_{ISM} (%)
Starbursts	0.1 (0.0–1.3)	4.3 (0.7–19.8)	93.3 (79.2–97.3)
LINER1	6.4 (0.6–36.7)	24.3 (16.2–60.4)	40.1 (22.2–74.3)
LINER2	3.5 (0.1–24.0)	36.0 (1.8–76.7)	51.6 (17.9–85.3)
Seyfert 1	77.2 (70.5–82.2)	14.3 (11.4–16.6)	9.4 (6.1–15.2)
Seyfert 2	58.2 (23.0–80.2)	10.9 (4.1–16.2)	30.7 (12.0–57.9)

those with RMSE > 0.3 (HC15). Ten objects show RMSE above that limit; two type-2 Seyferts (NGC 3393 and NGC 4945), two Starbursts (NGC 925 and NGC 3184), a type-1 LINER (NGC 4450), and five type-2 LINERs (IRAS 17208-0014, III Zw 035, IRAS 14348-1447, NGC 4125, and IRAS 12112+0305). Note that large RMSE values also imply a larger error on the estimates. We marked these sources in the plots in the following analysis. According to this criterion (RMSE < 0.3), DeblendIRS successfully fits the spectra in 90% of the sample. We have not found any trend on the quality of the fit according to the AGN classification. However, most of the objects with large RMSE are actually ULIRGs with deep silicate features (as already discussed by HC15).

5. Torus Contribution versus AGN Luminosity

We examine the relationship between $\log(L_{bol})$ and C_{torus} in Figure 5. C_{torus} is reported in Tables 1–3 (Col. 5). The bolometric luminosities are computed using the 2–10 keV luminosities (L(2–10 keV); reported in Tables 1, 2 and 3, Col. 4) using the relation $L_{bol} = \kappa$ L(2–10 keV), where the bolometric correction (κ) depends on the L(2–10 keV) luminosity itself with a fourth-order polynomial (see the prescription given by Marconi et al. 2004):

$$\log(\mathcal{L}/L(2\text{–}10\ \text{keV})) = 1.54 + 0.24\mathcal{L} + 0.012\mathcal{L}^2 - 0.0015\mathcal{L}^3, \quad (1)$$

where $\mathcal{L} = (\log L_{bol} - 12)$ and L_{bol} is in units of $L_{\odot}$.

5.1. Affinity Groups

Although there is a trend showing that less luminous objects have smaller C_{torus}, the relation between the bolometric luminosity and C_{torus} is not linear (coefficient of correlation $r = 0.6$). Figure 5 (left panel) shows the expected luminosity below which the torus would disappear (Elitzur & Shlosman 2006) as a red dashed vertical line. Indeed, objects below that limit tend to show small C_{torus}. Above that limit, there is a wide range of percentages of torus contributions C_{torus}. In order to quantify this (and also to define groups within the plot for subsequent analysis), we have used the clustering Affinity Propagation (AP) method (Frey & Dueck 2007) to look for groups in this diagram. Clustering analysis is aimed at discovering the underlying clusters in the data points according to their similarities. The AP method, in particular, is based on the concept of message passing between data points. The advantage of this method compared to other clustering methods (e.g., k-means) is that AP does not require the number of clusters as an input to the algorithm. The AP method divides the sample into groups and chooses one object as the representative of its group.

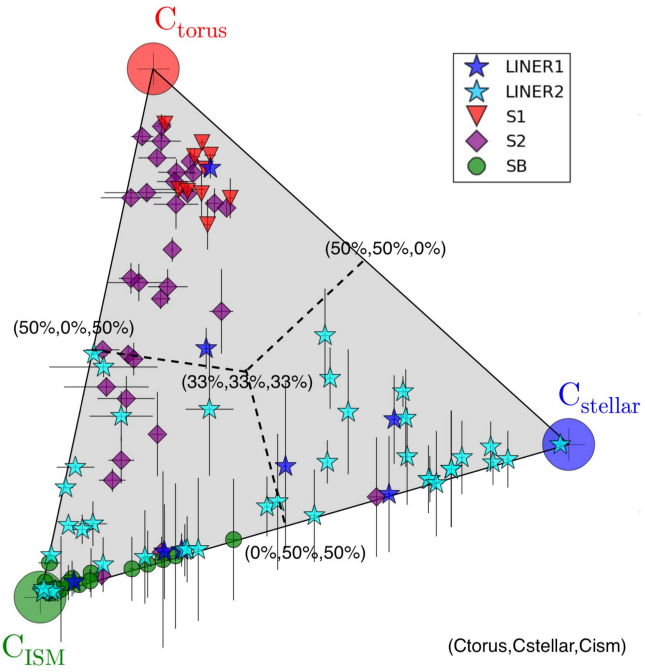

Figure 4. Diagram showing the contribution of the torus (top corner marked with the large red circle), ISM (bottom-left corner marked with the large green circle), and stellar (bottom-right corner marked with the large blue circle) components to the objects in our sample. Objects close to the corners of this triangle show large contributions of the corresponding component (see the text). Type-1 Seyferts, type-2 Seyferts, type-1 LINERs, type-2 LINERs, and Starbursts are shown with upside-down red triangles, purple diamonds, dark blue stars, light blue stars, and green circles, respectively.

We have applied the AP method to the pair of data [L_{bol}, C_{torus}] for the full sample using the Python routine "AffinityPropagation" within the package SCIKIT-LEARN.[12] We used "euclidean" as the affinity method, which uses the negative squared Euclidean distance between points. We set the maximum number of iterations *max_iter* to 1000 although the actual number of iterations needed to converge was only 43. The routine iterates until the number of estimated clusters does not change for a selected number of iterations *convergence_iter*. We set this number of iterations to *convergence_iter* = 15. Note that the *convergence_iter* parameter is a different restriction than *max_iter* parameter. However, we have noticed that changes in this *convergence_iter* parameter do not affect the results as long as *convergence_iter* > 1. This means that the groups in the sample were found after the second iteration.

Using the AP method, the points in Figure 5 (left panel) can be classified into five groups. Col. 10 in Tables 1–3 show which group each object belongs to. Table 7 gives the pair of positions for the representative member of each group and the median (and the 25th–75th percentiles as the width of the distribution) of the objects belonging to each group. The locus of the representative members and their median values are shown in the small inset within Figure 5 (left panel) as squares and black crosses, respectively. The main difference between groups is the percentage of the torus contribution, C_{torus}. Among them, only one group is below the line of $L_{bol} = 10^{42}$ erg s^{-1} and the median C_{torus} for them is consistent with zero ($C_{torus} < 1.4\%$; see Table 7). Furthermore, only three objects are consistent with this group but showing

[12] http://scikit-learn.github.io

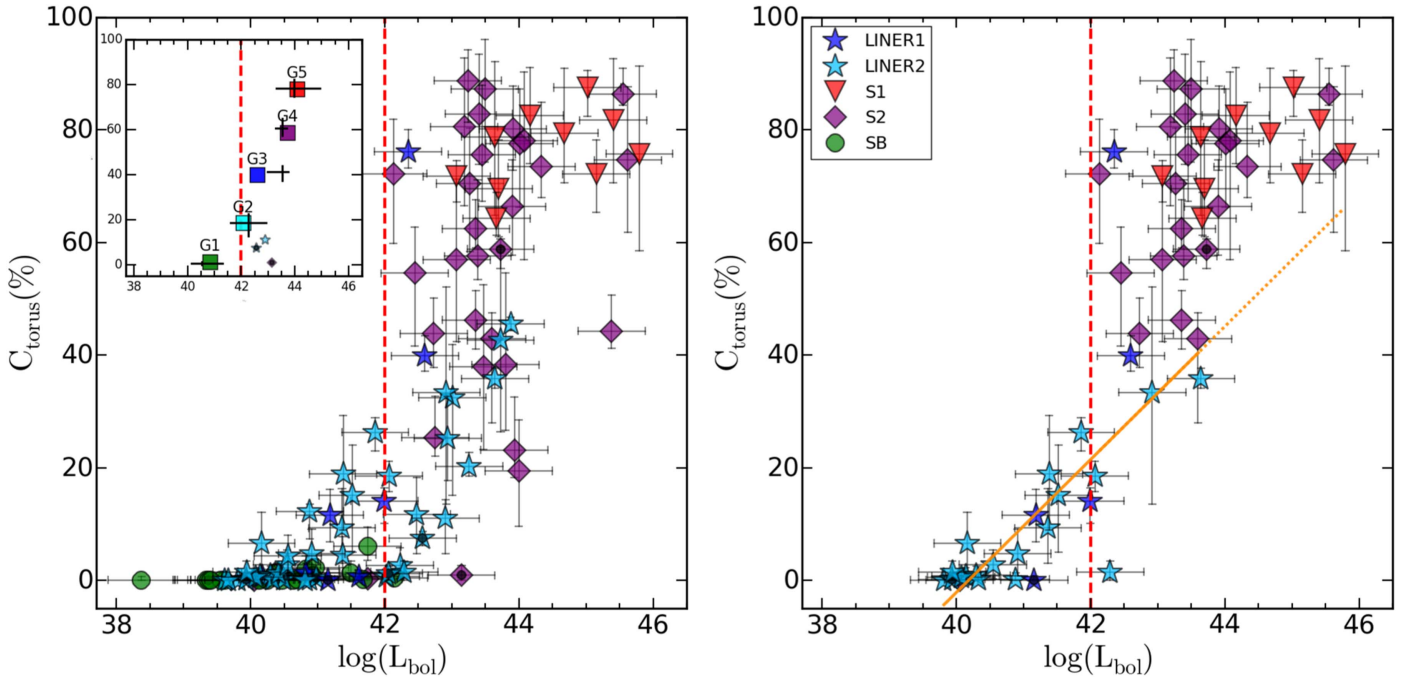

Figure 5. Contribution of the torus component vs. the bolometric luminosity (in units of erg s^{-1}) in logarithmic scale for the full sample (left) and for those showing $C_{ISM} < 50\%$ (right). The vertical dashed red line shows $L_{bol} = 10^{42}$ erg s^{-1}, the value where the torus is expected to disappear. However, note that this limit actually depends on the SMBH mass (Elitzur & Ho 2009; see also the text). The small inset within the left panel shows the representative objects for the five groups found using the AP method (see the text) with a square. It also shows the median values of the groups found using the AP method (errors show the range using 25th–75th percentiles). Objects with RMSE > 0.3 are marked with a black dot in both panels. Objects shown in this small box (left panel) are those consistent with the group that has negligible C_{torus} at mid-infrared and bolometric luminosities $L_{bol} > 10^{42}$ erg s^{-1} (NGC 4945 (S2), UGC 05101 (LINER2), and IRAS 14348-1447 (LINER2); see the text. The orange solid line (right panel) shows the best-fit linear relation for objects with $C_{torus} < 50\%$. The orange dotted line (following the orange solid line) is the extrapolation expected for larger bolometric luminosities.

$L_{bol} > 10^{42}$ erg s^{-1} (namely NGC 4945, UGC 05101, and IRAS 14348-1447, shown in the small panel in Figure 5, left panel). Among them, all but UGC 05101 have RMSE > 0.3, indicating poor decompositions. Thus, the behavior seen in Figure 5 is consistent with a wide range of C_{torus} above $L_{bol} = 10^{42}$ erg s^{-1} and negligible C_{torus} below that limit.

It is also worth mentioning the results of this classification method compared to the optical classes included in this analysis (see Col. 8 in Tables 1–3). All the Starbursts are classified as Group 1 (i.e., $C_{torus} < 1.4\%$; see Table 7). This is fully expected under the assumption that all these sources are non-AGNs. However, Group 1 also contains four type-2 Seyferts, four type-1 LINERs, and 25 type-2 LINERs. Eight out of the ten type-1 Seyferts are classified within Group 5 (i.e., $C_{torus} \simeq 80\%$; see Table 7). Only one LINER (NGC 1052) and 11 type-2 Seyferts are associated with Group 5. Except NGC 1052, all LINERs belong to groups below Group 3. In the case of Seyferts, there is a complete mix of groups.

The measurement of C_{torus} could depend on the host galaxy properties. We have collected the morphological types and B magnitudes[13] for the galaxies in our sample and studied whether the distribution changes with the AP groups. We have computed the 25th–75th percentiles of each distribution for morphological types and B magnitudes (these numbers are recorded in Table 7). There is an increase on the B total magnitude from Group 1 to Groups 4–5, although all of them agree with each other within the percentiles. Furthermore, more distant objects could also include more dust within the slit of *Spitzer*/IRS. We also computed the 25th–75th percentiles of each distribution of "Slit widths" (see Table 7). There is no correlation between the AP groups and the physical portion of the galaxy included in the IRS slit width.

We have investigated if the percentage of ISM contribution (C_{ISM}) might affect our results. $C_{ISM} > 50\%$ for Starbursts. This is consistent with the idea that the PAH features dominating the ISM are produced in the photodissociating region associated with a star-forming region. Starbursts, essentially H II galaxies, are dominated by star-forming regions all over the SED, and therefore, dominated by the PAH features at the mid-infrared. Among the AGN classes, both LINERs and Seyferts are spread in a wide range of C_{ISM}. This is consistent with the idea that C_{ISM} depends on the inner star formation (~1 kpc). Indeed, we have studied whether this contribution depends on AGN luminosity, finding no correlation at all ($r = 0.18$).

We have examined how Figure 5 (left panel) changes if we consider only objects with $C_{ISM} < 50\%$ (see Figure 5, right panel). Now the tendency toward a large C_{torus} for larger AGN bolometric luminosities is much clearer ($r = 0.8$). This correlation is still better ($r = 0.9$) if we select objects with $C_{torus} < 50\%$ (see the solid orange line in Figure 5, right panel). Furthermore, it is worth noting that objects with $C_{torus} > 50\%$ do not follow the same relation (only two objects are consistent within the error bars). In fact, they tend to have a larger C_{torus} than that expected from the extrapolation of the linear fit of objects with $C_{torus} < 50\%$ (dotted orange line in Figure 5, right panel).

[13] Note that in the case of the B magnitudes we found them for 80 sources in our sample.

Table 7
Overall Results of the Affinity Propagation (AP) Clustering Method

Group	Representative Member		Median of the Group		Morph.	Slit Width log(pc)
	$\log(L_{bol})$	C_{torus}	$\log(L_{bol})$	C_{torus}		
1	40.8	1.3	40.5 (40.1, 41.3)	0.6 (0, 1.4)	2 (0, 5)	2.6 (2.4, 2.8)
2	42.1	18.5	42.5 (41.9, 43.0)	18.8 (14.1, 23.0)	1 (−1, 3)	2.8 (2.6, 3.1)
3	42.6	39.8	43.5 (43.0, 43.7)	41.2 (37.4, 43.9)	2 (−3, 2)	3.1 (2.9, 3.4)
4	43.7	58.8	43.5 (43.2, 43.7)	60.6 (57.4, 64.8)	1 (0,1)	2.8 (2.7, 3.0)
5	44.1	78.0	44.0 (43.3, 45.0)	78.4 (74.9, 82.3)	1(−2, 4)	3.0 (2.7, 3.2)

Note. The confidence levels computed for the median values are the 25th–75th percentiles; they are not an error on the estimates.

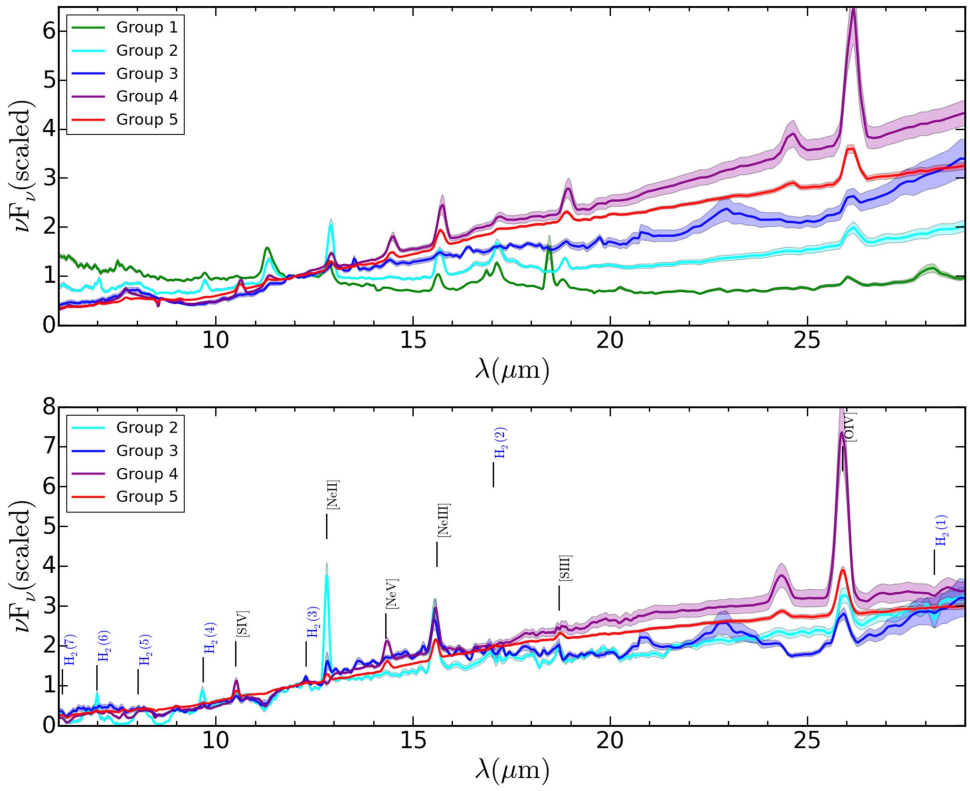

Figure 6. Top: Average *Spitzer*/IRS spectra for the groups found using the AP method with $C_{ISM} < 50\%$ (see the text). (Bottom): Same average *Spitzer*/IRS spectra as in the top panel but after subtracting the ISM and stellar components (i.e., the AGN component). Note that we do not show Group 1 because the AGN component is only a residual (see the text). H_2 molecular lines are marked with blue letters and forbidden transitions are shown in black letters.

5.2. Average Spectra

We constructed an average spectrum for each of the five groups found using the AP method (see Figure 6, top panel). The dispersion shown as a shadow area is the 1σ uncertainty of the mean. All the spectra are scaled to their flux at 12 μm before averaging. As in Figure 5 (right panel), we have excluded objects with $C_{ISM} > 50\%$ to avoid those spectra where the ISM is dominating the observed emission.[14] The slope of the spectra gradually becomes bluer as we move to lower C_{torus} (i.e., as we move from Group 4 and 5 to Group 1). We interpret this as stellar dominance for the observed first AP classes ($C_{torus} < 40\%$). Our decomposition method allows us to study the average spectrum by isolating the torus component for each AP group. For that purpose, we have subtracted the stellar and ISM components from the *Spitzer*/IRS spectra. The average spectra are shown in Figure 6 (bottom panel). We do not show in this plot the average spectrum for Group 1 ($C_{torus} < 1.4\%$) because, after removing stellar and ISM spectra, the residuals are negligible in this group (see Table 7). Now the average spectra are much more similar among the four groups. The main difference is the presence of strong emission lines in Group 2. Indeed, while collisional lines such as [S IV], [Ne II], [Ne III], and [O IV] are present in all the categories, it seems that there is an enhancement of the H_2 molecular lines in Groups 2 and 3 ($C_{torus} \sim 20\%$ and $C_{torus} \sim 40\%$, respectively).

It is worth mentioning that Group 2 (2, 3, and 4) show the H_2 molecular line at 28 μm (PAH feature at 11.3 μm) in absorption. This indicates a slight oversubtraction of those emission lines. However, note that all the other H_2 molecular

[14] We have excluded objects with large contributions of ISM because all AGN classes show a large range of ISM contributions, indicating that this component is independent of the AGN classes and entirely due to the circumnuclear conditions of each source.

lines are shown in emission and that the other PAH features (e.g., 8.7 μm) are not seen in either emission or absorption. Thus, we believe this oversubtraction depends on the particular conditions of the lines. Perhaps this oversubtraction of the H_2 molecular lines could indicate a different composition of the clouds. In the case of PAH features, it is even harder to evaluate since changes in the composition of PAHs could yield to a different profile of this line.

We have fitted the subtracted average spectra (Figure 6, bottom panel) with the Clumpy torus models (Nenkova et al. 2008a, 2008b) using Bayesian inference to estimate probability distributions for the parameters of the torus model. Note that emission and absorption features have been removed from the spectral coverage since these models only account for the shape of the continuum. The BayesClumpy code uses the Metropolis–Hastings Markov Chain Monte Carlo algorithm for sampling the posterior distribution function (see Asensio Ramos & Ramos Almeida 2009 for more details on the code). The parameters of the torus involved in the fitting are the half opening angle of the torus σ, the outer radius of the torus as a function of the inner radius of the torus $Y = R_{\rm out}/R_{\rm inner}$, the number of clouds in the equatorial plane $N_{\rm o}$, the slope of the power-law distribution of clouds with respect to the angle from the equatorial plane q, the optical depth of the clouds τ_ν, and the inclination between the line of sight and the equatorial plane of the torus i. Using the best-fit parameters, BayesClumpy marginalizes over the AGN geometrical covering factor, f_C:

$$f_c = 1 - \int_0^{90^\circ} e^{-N_o e^{-(90^\circ - i)^2/\sigma^2}} \cos(i) di. \quad (2)$$

The inner radius of the torus is linked to the AGN bolometric luminosity because it depends on the radius at which the dust sublimates (see Barvainis 1987; Nenkova et al. 2008a, 2008b). Thus, the outer radius of the torus can be computed using the bolometric luminosity of the AGN and the parameter Y. The height of the torus H can also be computed as $H = (R_{\rm out} + R_{\rm in})\sin(\sigma)/2$.

We did not fit Group 1 because after subtracting the stellar and ISM components, only residuals are left. Figure 7 shows the best fit for Groups 2, 3, 4, and 5. We failed to find a good fit for Group 2. Although the average spectrum of Group 2 resembles Groups 3, 4, and 5, below 10 μm it decreases with a slope too steep and it increases too quickly above 25 μm for any of the Clumpy models. We believe that the extra contribution above 25 μm could be a residual of the ISM component. The deficit of emission compared to the model below 10 μm could be due to extra extinction or due to a distribution and/or composition of the dusty region not predicted by the Clumpy models described by Nenkova et al. (2008a, 2008b).

We were able to successfully fit Groups 3, 4, and 5, although the spectral fitting for Group 3 is visually worse than that for Groups 4 and 5. The resulting parameters are listed in Table 8. All the parameters are in the range found for AGNs fitted with Clumpy models (Nenkova et al. 2008b; Ramos Almeida et al. 2009, and references therein). Torus sizes recovered by the models are fully in agreement with mid-infrared interferometric observations (Burtscher et al. 2013).

Rather than focus on the actual numbers obtained for each group, it is more relevant to look for differences in the measured parameters among the three groups. The number of clouds in the equatorial plane ($N_{\rm o}$) and the viewing angle (i) is similar for the three groups. However, when we split Group 5 into type-1 and type-2 AGNs[15] (see the last two columns in Table 8), we naturally recover the dependence on the viewing

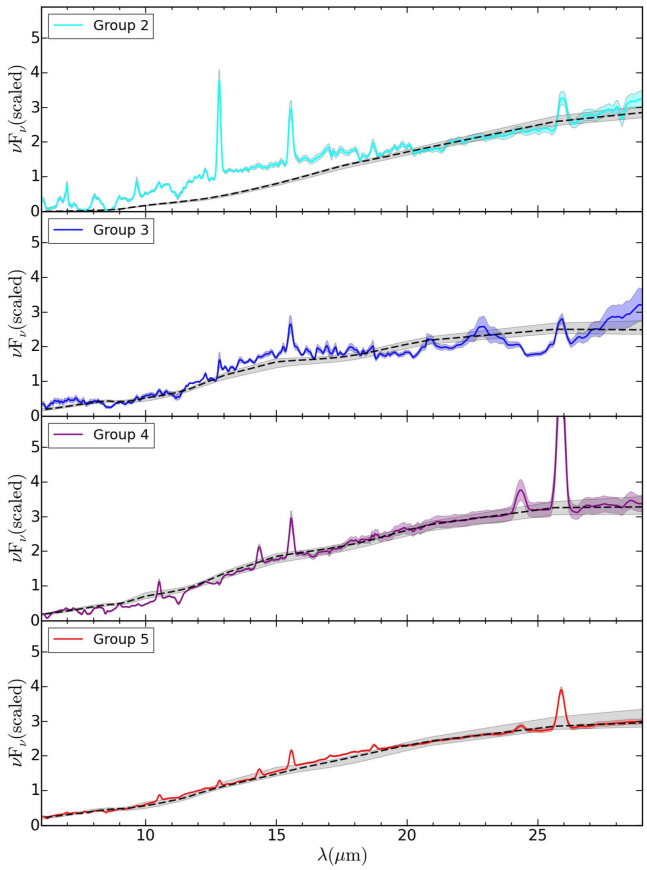

Figure 7. Clumpy model fits (long dashed black lines) to the average AGN component of Groups 2, 3, 4, and 5 (from the top to the bottom panel). The gray shadowed region is the lower and upper bounds of the fit.

Table 8
Parameters of the Clumpy Models Obtained using the Code BayesClumpy

Param.	Group 3	Group 4	Group 5		
($C_{\rm torus}$)	(40%)	(60%)	(80%)		
			All	Type 1	Type 2
σ	52^{+9}_{-11}	48^{+12}_{-13}	38^{+19}_{-14}	36^{+15}_{-11}	35^{+17}_{-7}
Y	$13.2^{+2.8}_{-2.0}$	$14.6^{+4.2}_{-2.0}$	$21.0^{+7.7}_{-3.1}$	27^{+26}_{-8}	$22.0^{+5.3}_{-2.8}$
$R_{\rm in}$ (pc)	0.025	0.089	0.14	0.14	0.14
$R_{\rm out}$ (pc)	$0.33^{+0.07}_{-0.05}$	$0.82^{+0.23}_{-0.11}$	$2.36^{+0.84}_{-0.34}$	$3.0^{+2.8}_{-0.9}$	$2.42^{+0.31}_{-0.58}$
H (pc)	$0.14^{+0.05}_{-0.05}$	$0.34^{+0.14}_{-0.14}$	$0.76^{+0.45}_{-0.45}$	$\sim$0.9	$\sim$0.7
$N_{\rm o}$	$6.3^{+2.9}_{-1.5}$	$6.5^{+3.3}_{-1.7}$	$7.0^{+3.6}_{-2.2}$	$6.7^{+3.8}_{-2.8}$	$8.5^{+3.5}_{-2.5}$
q	$0.39^{+0.45}_{-0.25}$	$0.61^{+0.72}_{-0.40}$	$0.72^{+0.68}_{-0.46}$	$1.26^{+0.46}_{-0.56}$	$0.56^{+0.58}_{-0.36}$
τ_ν	71^{+25}_{-18}	110^{+21}_{-25}	64^{+27}_{-24}	42^{+32}_{-16}	43^{+21}_{-17}
i	58^{+18}_{-32}	60^{+16}_{-24}	65^{+13}_{-26}	35^{+22}_{-21}	73^{+9}_{-14}
f_C	$0.74^{+0.13}_{-0.24}$	$0.67^{+0.16}_{-0.24}$	$0.48^{+0.26}_{-0.29}$	$0.42^{+0.22}_{-0.18}$	$0.45^{+0.27}_{-0.14}$

Note. $R_{\rm in}$ is estimated from the bolometric luminosity, $R_{\rm out}$ is estimated from $Y\,R_{\rm in}$, H(pc) is estimated using $R_{\rm out}$, $R_{\rm in}$, and σ, and f_C is estimated using the other parameters with Equation (2). Group 1 was not fitted. We did not find a good fit for Group 2 (see text). We have also fitted the average spectrum of type-1 and type-2 Seyferts included in Group 5 (see the text).

[15] Note that this exercise can only be made in Group 5 because it is the only one containing type-1 Seyferts.

angle (as expected under the unified model). There is a marginal trend for an increase of the slope of the cloud distribution q with the distance from the equatorial plane, the height of the torus, and a decrease on the half opening angle σ from Group 3 to Group 5. The latter results in a marginal detection on higher geometrical covering factors for lower luminosity AGNs.

The parameter that is changing the most among the three groups is the outer size of the torus ($R_{\rm out}$), increasing from Group 3 to Group 5 (i.e., for $C_{\rm torus}$ from 40% to 80%). Alonso-Herrero et al. (2011) did not find a different size of the torus, fitting 13 AGNs to the very same Clumpy models used here. However, there are two main reasons why these results are not in contradiction. First, the range of luminosities covered here is much larger than those reported in their sample. Indeed, the sizes of the torus and bolometric luminosities reported in their publications are consistent with all of them being mainly in Group 5. Second, we have found this tendency after averaging objects classified into the same group using the AP method while they used individual Clumpy fits to derive their conclusions. Since the torus half opening angle (σ) is similar and the size of the torus ($R_{\rm out}$) is smaller when moving from Group 5 to Group 3, the covering factor (the half opening angle of the torus) of the AGN is larger (smaller) for Group 3 compared to Group 5. Note that far-infrared flux observations would be more sensitive to the torus extent independently (Ramos Almeida et al. 2011). Thus, the addition of these measurements could confirm the trend found here for the AP groups (i.e., with $C_{\rm torus}$).

5.3. Warm Molecular Gas

Motivated by the H_2 molecular emission lines detected in Groups 2 and 3 found using the AP method, we have done a search for all the H_2 molecular lines found in the *Spitzer*/IRS spectra of the sample. Due to the coverage of our spectra, we have been able to look for the transitions S(0) 28.22 μm, S(1) 17.03 μm, S(2) 12.27 μm, S(3) 9.67 μm, S(4) 8.02 μm, S(5) 6.91 μm, and S(6) 6.11 μm. We have built a code using Python routines (within SCIPY) to automatically detect these lines. We have forced a fit to a Lorentzian profile to each of the proposed lines. We allowed the amplitude, center, and width of the Lorentzian profile to vary. We have run this fitting 200 times using Monte Carlo simulations to estimate the error of these fittings from the error of each spectrum. We consider a line to be detected if the amplitude of the line is above three times its error and the center of the line is consistent with the expected wavelength of the line within the width of the Lorentzian. Note that we have performed such a detection in the *Spitzer*/IRS spectra and not after the stellar and ISM components were subtracted.

We have not detected S(0) in any of the objects of our sample. Furthermore, none of the H_2 molecular lines are detected in any of the Starbursts and type-1 Seyferts included in our comparison sample. S(5) and S(6) lines are detected among both LINERs and type-2 Seyferts. S(4) is detected only in five objects, three in Group 1 and two in Group 5. S(1), S(2), and S(3) are only detected in Groups 1, 2, and 3 (i.e., $C_{\rm torus} < 40\%$).

6. Discussion

An outflowing wind of material from the AGNs might be responsible for the BLR, NLR, and torus components (e.g., Elitzur & Ho 2009 and references therein). According to Emmering et al. (1992), the properties of these components depend on the AGN bolometric luminosity (see also Nicastro 2000). Many evidences for cloud outflows indicate that instead of a hydrostatic torus, this region is part of a clumpy wind (including BLR and NLR) coming off the accretion disk (Emmering et al. 1992; Nicastro 2000; Wada 2012, and references therein). Indeed polar dust emission is being found in some AGNs, with a P.A. coincident with that of the NLR or the jet (Mor et al. 2009; Asmus et al. 2016; López-Gonzaga et al. 2016). Detailed fitting of the SED including dust from both NLR and torus has been presented (Elitzur & Shlosman 2006; Mor et al. 2009; Mor & Netzer 2012). The inner radius of the torus depends on the luminosity (Lawrence 1991), giving a dependence on the covering factor for a fixed torus half opening angle (the so-called receding torus; Gopal-Krishna et al. 1996; Willott et al. 2000; Simpson 2003; Arshakian 2005). Furthermore, at the very low-luminosity end, this torus is expected to disappear (Elitzur & Ho 2009; Elitzur 2012; Elitzur & Netzer 2016, and references therein).

We indeed find a marginal evolution of the covering factor as the AGN bolometric luminosity decreases (see Table 8). As shown in the previous section, the geometrical covering factor depends on the equatorial number of clouds (N_0) and on the half opening angle. In this case, this marginal increase on the geometrical covering factor comes from a marginal increase on the half opening angle toward lower luminosities. Simpson (2005) already proposed a slight modification of the receding torus model based on a new analysis of the fraction of type-1 versus type-2 AGNs, where the height of the torus also increases when AGN ionizing luminosity increases. Indeed, we have found a marginal increase on the height of the torus when the bolometric luminosity increases. A more robust result is that the outer radius of the torus size might also depend on the AGN bolometric luminosity. Clumpy models associated with Groups 3, 4, and 5 show that the outer radius of the torus seems to increase as the bolometric luminosity of the AGN (and $C_{\rm torus}$) increases. The main difference in these groups is the $C_{\rm torus}$, which is 40%, 60%, and 80% respectively. Thus, it might indicate that the dust contributing within the *Spitzer*/IRS slit associated with the torus component ($C_{\rm torus}$) is increasing mainly because the size of the torus is increasing. The stratification of H_2 molecular lines detected in this analysis is also interesting. While S(5) and S(6) transitions are seen in all the AP groups, S(1), S(2) and S(3) transitions are only detected in Groups 1, 2, and 3 (i.e., $C_{\rm torus} < 40\%$). This was already reported by Panuzzo et al. (2011) in their Class-2 objects (those showing PAH features with anomalous 7.7/11.3 μm PAH ratios). Each of these molecular lines could be tracing different densities and/or temperatures of the molecular gas content (see Roussel et al. 2007). Thus, independently of the origin of these lines, this result is more likely related to changes in the density and temperatures of the gas clouds. The gas could also be changing its content and distribution, coupled with the dust, if the dust is changing its morphological distribution. Supporting this, a more concentrated molecular gas distribution toward the center was reported for three LLAGNs by Müller-Sánchez et al. (2013), compared to Seyferts, using integral field spectroscopy in the near-infrared. They argued that this change of the concentration of molecular gas is related with the progressive disappearance of the torus. Alternatively, the change of the configuration of the dust or the AGN power allows the AGN to

heat the gas to farther distances, resulting in an enhancement of some particular transitions of the H_2 molecular line. Finally, clumpy torus models applied to the different groups found by the AP method show that Group 2 (i.e., $C_{\rm torus} \sim 20\%$) is no longer reproduced (although it visually resembles) by clumpy torus models, suggesting also a different composition or structure of clumps for this group. As a speculation, these results might suggest a smooth transition from higher to lower AGN luminosities with changes in temperature, density, and/or location of the dust and gas surrounding the AGN, until the disappearance of the torus. These changes in the torus characteristics are predicted by Hönig & Beckert (2007), based on stability arguments (i.e., gravity versus radiation pressure produced by the accretion disk). They showed that at $L_{\rm bol} < 10^{42}$ erg s^{-1} and according to the clumpy torus model, the torus collapses to a geometrically thin disk. Thus, the mid-infrared emission below that limit is not produced by the geometrically thick torus.

Note here that we are not excluding the viewing angle as a cause for some of the AGN classes. Indeed, when we split Group 5 into type-1 and type-2 AGNs, the viewing angle plays an important role (see Table 8). However, as long as we move toward low luminosities, intrinsic differences in the outer radius of the torus or the molecular gas distribution must be taken into account to produce a clear picture of AGNs and their evolution from (or to) a non-active galaxy. Note also that these results are found assuming that the torus is clumpy. A detailed analysis of the clumpy versus smooth distribution of the torus, perhaps through the relative strength of the 10 and 18 μm silicate features, is also needed (Sirocky et al. 2008; Hatziminaoglou et al. 2015; Mendoza-Castrejón et al. 2015). However, the large ISM contributions in our *Spitzer*/IRS spectra (see Section 4.2) prevent us from analyzing the silicate features because they are highly contaminated by this contribution.

An expected dependence of the torus on luminosity is the disappearance of the torus below a certain bolometric luminosity (Elitzur & Shlosman 2006). The reason is that the accretion onto the SMBH can no longer sustain the required cloud outflow rate. González-Martín et al. (2015) found some evidence in favor of the disappearance of the torus below the bolometric luminosity $L_{\rm bol} \sim 10^{42}$ erg s^{-1}. The mid-infrared spectrum of AGNs with $L_{\rm X} < 10^{41}$ erg s^{-1} showed a completely different shape compared to brighter AGNs. However, the main concern for the latter study is that *Spitzer*/IRS spectra have low spatial resolution. Thus, many ingredients other than the AGN can contribute to the mid-infrared emission. Therefore, galaxy dilution could still play a role. The idea is that the torus does not disappear but it gets diluted due to the lower torus contribution compared to the host galaxy. This naturally explains the linear relation between $C_{\rm torus}$ and bolometric luminosities for intermediate luminosities (orange solid line in the left panel of Figure 5; see Section 5). Although we cannot rule out this scenario, we believe it is less plausible because we would expect this relation to continue toward higher bolometric luminosities. Instead, we find that high luminosity AGN tend to show larger $C_{\rm torus}$ than expected for the linear relation. Alternatively, this relation is also expected under the evolutionary scenario in which the star formation increases when the AGN bolometric luminosity decreases. In this scenario, the contribution of the torus decreases due to an enhancement of the ISM contribution. However, the increase in the star formation for LLAGNs is in contradiction with other results. Most of the LLAGNs are hosted in elliptical galaxies (Carrillo et al. 1999), where there is a lack of young stars. Furthermore, young stellar populations are almost negligible in the circumnuclear environment of LLAGN, mainly constituted by old stars (Cid Fernandes et al. 2004; González Delgado et al. 2004, 2008; Sarzi et al. 2005). Indeed, Krongold et al. (2003) discussed the possibility that strong winds of Wolf Rayet and O stars wipe out the circumnuclear material left over from an initial circumnuclear star formation in LINERs. Thus, this is a less preferred scenario to explain the $C_{\rm torus}$ versus $L_{\rm bol}$ relation.

On the other hand, if the torus disappears, we would expect $C_{\rm torus} \sim 0\%$ below a certain luminosity. This is consistent indeed with our findings, where Group 1 shows $\log(L_{\rm bol}) < 41.3$ and $C_{\rm torus} < 1.4\%$ (see Table 7). Another way to compute the luminosity limit where the torus is disappearing is to make a linear fit to $L_{\rm bol}$ versus $C_{\rm torus}$ for Groups 3, 4, and 5, extrapolating the $L_{\rm bol}$ limit when $C_{\rm torus} = 0\%$. This is, according to our observations, $\log(L_{\rm bol}({\rm erg\ s^{-1}})) = 41.2$, which is fully consistent with Group 1. This luminosity limit is below that inferred by González-Martín et al. (2015), i.e., $\log(L_{\rm bol}) \simeq 42$. This discrepancy is due to the fact that their limit was imposed to compute the average spectra while the current limit is computed from observations. This limit is well below that predicted by Elitzur & Shlosman (2006), i.e., $\log(L_{\rm bol}({\rm erg\ s^{-1}})) \sim 42$. However, Elitzur & Ho (2009) updated it, finding that it depends on the SMBH mass as $L_{\rm bol} = 5 \times 10^{39}(M/10^7 M_\odot)^{2/3}$ erg s^{-1}. Assuming that the disappearance of the torus corresponds to the largest SMBH masses (LLAGNs tend to have the largest SMBH masses, i.e., $M = 10^9 M_\odot$), the bolometric luminosity limit is $\log(L_{\rm bol}({\rm erg\ s^{-1}})) \simeq 41$, consistent with our findings.

To explore more carefully the dependence of the minimum AGN bolometric luminosity (required to hold the outflowing structure) on the SMBH mass, we have compiled the available SMBH masses in the literature for 85 of the 109 objects in our sample (Woo & Urry 2002; González-Martín et al. 2009a; McKernan et al. 2010; González-Martín & Vaughan 2012; Zoghbi et al. 2014; Bentz & Katz 2015, and references therein). Figure 8 shows the AGN bolometric luminosity versus the SMBH masses in our sample. Smaller symbols show objects with $C_{\rm ISM} > 50\%$ and larger symbols show objects with $C_{\rm ISM} < 50\%$.

Elitzur & Netzer (2016) show that the minimum AGN bolometric luminosity depends on the combination of several parameters of the wind (the radiative conversion efficiency, the ratio between the SMBH accretion rate and the wind accretion rate, and a factor I that depends on the ratio between the outflow launch velocity and the local Keplerian velocity and the radial density variations). For a certain SMBH mass, there is a limit on the bolometric luminosity below which they do not expect any BLR or torus to survive (shown as the red solid line in Figure 8). Moreover, there is an upper limit above which the BLR and the torus must be present (shown as the gray solid line in Figure 8). In the range between the upper and the lower limits, both scenarios could happen.

The 14 LLAGNs where the torus seems to have disappeared according to our analysis are marked with ♣ in Tables 1–3 and are shown with small black dots in Figure 8. The red shaded area shows the area where the wind radial column drops below the minimum required to produce detectable BLRs and dusty tori according to Elitzur & Netzer (2016). All the objects in this area are candidates for the disappearance of the torus according to our analysis. The only exception is NGC 5866. It was not

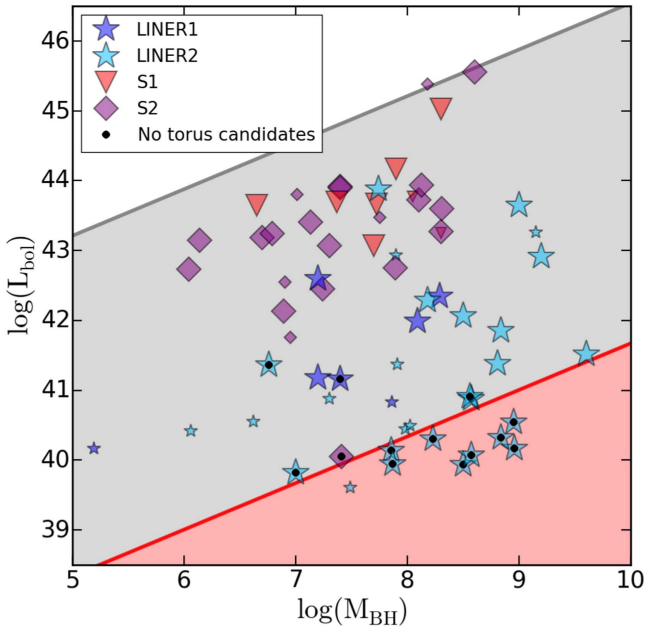

Figure 8. AGN bolometric luminosity $L_{\rm bol}$ vs. the SMBH masses, both in logarithmic scales. Smaller (larger) symbols show objects with $C_{\rm ISM} > 50\%$ ($C_{\rm ISM} < 50\%$). Red and gray solid lines show the lower and upper limits on the AGN bolometric luminosity for the disappearance of the torus, according to Elitzur & Ho (2009). The torus is no longer present in the red shaded area and the torus might disappear only for certain combinations of the wind parameters in the gray shaded area (see the text).

included in our list of candidates because it shows large contributions from the ISM but still shows $C_{\rm torus} < 0.7\%$. Two objects (and another four very close to the lower limit of the bolometric luminosity; red solid line in Figure 8) are in the gray shaded area of the plot. Elitzur & Netzer (2016) showed that only some sources in this gray shaded area might not have a torus depending on the combination of parameters of the outflowing wind. Thus, our findings are in agreement with the most recent prediction of the disappearance of the torus presented by Elitzur & Netzer (2016).

Figure 9 shows a schematic view of the tori for Groups 3, 4, and 5 (from left to right), according to the best fit to the Clumpy torus models (Table 8). The top panels show the tori for the three groups in a box with a fixed side of 4.6 pc. This clearly shows how drastically the outer radius and height of the torus decreases toward lower luminosities. This tendency seems to evolve to its disappearance at bolometric luminosities of $\log(L_{\rm bol}\,({\rm erg\ s^{-1}})) \simeq 41$. The bottom panels in Figure 9 show the same schematic view of the tori for Groups 3, 4, and 5 but optimizing the size of the box to match the outer size of the torus. The half opening angle slightly increases toward lower luminosities, being responsible for the tentative increase of the geometrical covering factor. Although larger covering factors and smaller torus sizes seem to be contradictory, this figure illustrates how both can coexist.

Figure 9 also shows, as a projection at the bottom of each panel, the radial profile of the number of clouds per unit length at the equatorial plane, $N_C(r,\,\beta = 0)$:

$$N_C(r,\,\beta = 0) = C\,N_o\,(R_{\rm in}/r)^q, \qquad (3)$$

where C is the normalization to guarantee that the number of clouds at the equatorial plane along any ray is $N_{\rm o}$ (i.e., $\int N_C(r,\,\beta = 0)dr = N_{\rm o}$). The distribution of the number of clouds per unit of length also seems to be different for Groups 3, 4, and 5. Group 3 shows the largest maximum values and a wider distribution of clouds, and Group 5 shows the lowest values and a narrower distribution of clouds. This shows the effect on the change of the q parameter on the structure of the torus.

It is worth emphasizing that our result on the plausible disappearance of the torus is not in contradiction with the 2–10 keV X-ray versus mid-infrared luminosity correlation found for AGNs by several authors (Krabbe et al. 2001; Lutz et al. 2004; Horst et al. 2006; Ramos Almeida et al. 2007; Horst et al. 2008; Gandhi et al. 2009; Asmus et al. 2011, 2014, 2015; Mason et al. 2012; González-Martín et al. 2013; García-Bernete et al. 2016). The deepest sample ever put together to study this correlation was presented by Asmus et al. (2014) and the X-ray to mid-infrared luminosity relation was analyzed by Asmus et al. (2015). They found a good correlation down to 2–10 keV X-ray luminosities of $\log(L_{\rm X}\,(2\text{–}10\ {\rm keV})) \simeq 40 (\log(L_{\rm MIR}\,(12\ \mu{\rm m})) \simeq 39.5)$. This correlation is being interpreted as an indication that both are tracing the same mechanism through reprocessed UV emission by the torus. Thus, the torus must be present up to these luminosities. The limit found in our paper is $\log(L_{\rm bol}\,({\rm erg\ s^{-1}})) \simeq 41.3$ (from AP analysis). This implies $\log(L_{\rm X}\,(2\text{–}10\ {\rm keV})) \simeq 40.1$, assuming a conversion $L_{\rm bol} = 15.8 \times L_{\rm X}\,(2\text{–}10\ {\rm keV})$ (Ho 2009). Only seven sources are below that limit in the correlation given by Asmus et al. (2015; namely Fornax, NGC 1553, NGC 4111, NGC 4278, NGC 4374, NGC 4395, and NGC 4594). In two cases they did not detect mid-infrared emission (NGC 1553 and NGC 4374), consistent with the lack of a torus for these sources. Three other sources (Fornax, NGC 4111, and NGC 4278) might be above $\log(L_{\rm X}\,(2\text{–}10\ {\rm keV})) \simeq 40.1$, considering the error bars of the X-ray luminosities. Thus, only two sources are consistent with being in the correlation and below the limit where the torus seems to disappear, namely NGC 4395 and NGC 4594. NGC 4395 is a strongly variable X-ray source (Cameron et al. 2012 and references therein). Its intrinsic X-ray luminosity could change by a factor of two, which already places this source above our limit. Indeed, variability is being discussed as a source of dispersion in this correlation (Mayo & Lawrence 2013). NGC 4594 (Sombrero Galaxy) shows a dust lane within the disk of the galaxy. It is plausible, although we cannot guarantee it, that this dust lane is contributing to the mid-infrared emission, even with high-resolution data. Mason et al. (2012) studied the behavior of this correlation for LLAGNs using high spatial resolution mid-infrared data. Only NGC 4736 has an X-ray luminosity below the expected limit for the disappearance of the torus (after taking into account the Compton thickness and X-ray variability). Interestingly, this object appears out of the X-ray to mid-infrared relation, as expected if it lacks the torus. Finally, no point-like nuclear sources are detected in high spatial resolution CanariCam data (Table 4) below that limit. We would like to remark that this is a limitation with the current ground-based mid-infrared instrumentation. Thus, new generation telescopes, going toward very low luminosities, are needed to confirm or reject the prediction of the torus disappearance with high spatial resolution imaging.

González-Martín et al. (2009b) showed that a large percentage (>40%) of their LLAGNs are Compton-thick candidates, i.e., with hydrogen column densities $N_{\rm H} > 2 \times 10^{24}\ {\rm cm^{-2}}$. This might be in contradiction with our findings of the lack of a torus

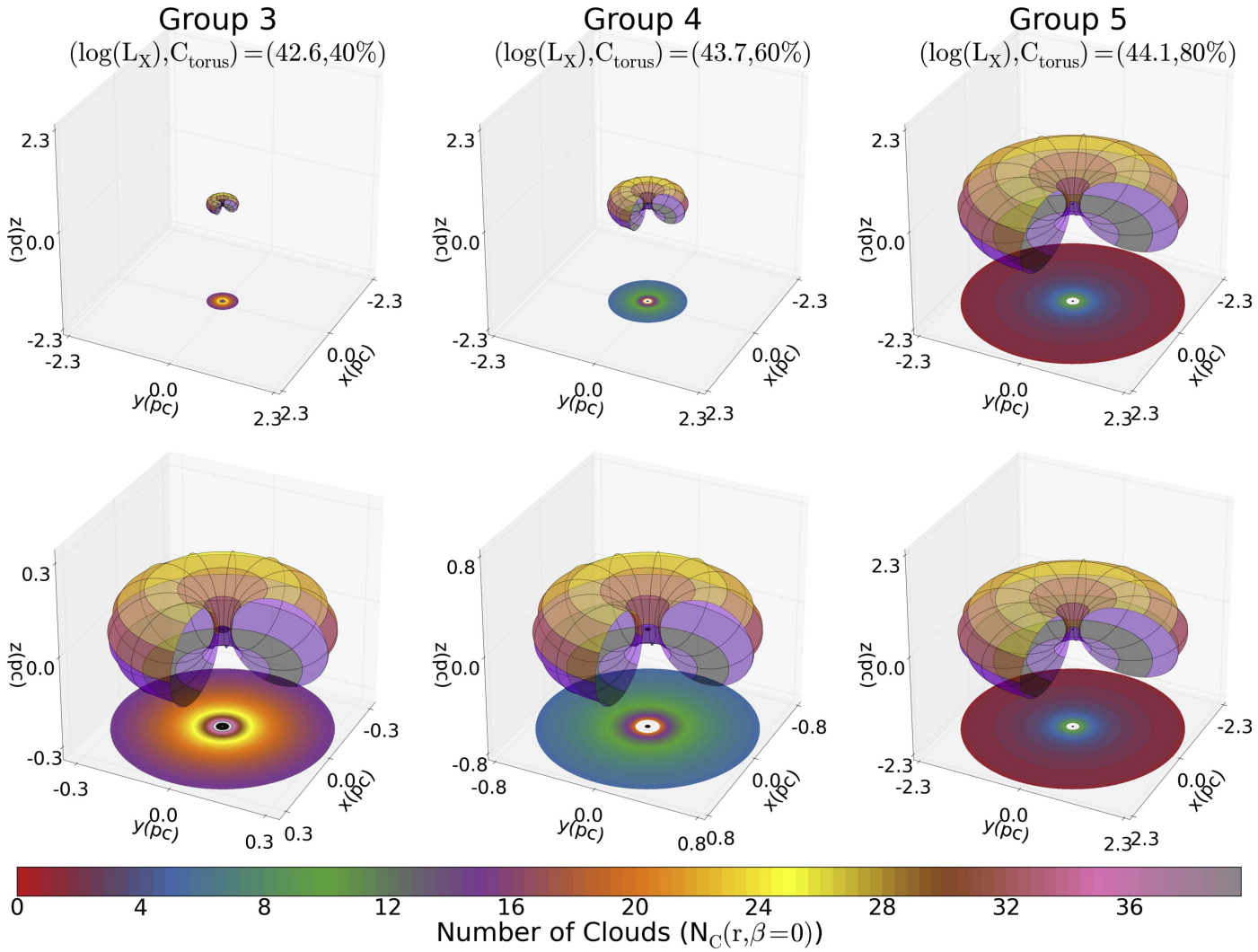

Figure 9. Schematic view of the tori for Groups 3 (left), 4 (middle), and 5 (right) using the best-fit parameters obtained with Clumpy models (see Table 8). We used a fixed size for the box of 4.6 pc in the top panels and the diameter of each torus (i.e., ∼0.7, 1.6, and 4.6 pc for Groups 3, 4, and 5, respectively) in the bottom panels. We also added a disk component only for viewing purposes with a radius of 0.2 pc as a toroidal structure with a half opening angle of $\sigma = 5°$ (i.e., this disk component does not have a realistic size). The projection seen at the bottom of each box shows the radial profile of the number of clouds at the equatorial plane (N_C; see the text).

for some of them. Eleven of these 14 LLAGNs are included in González-Martín et al. (2009b). Among them, only NGC 4589 is classified as a Compton-thick candidate. From the 40 LINERs classified as Compton-thick candidates in González-Martín et al. (2009b), only another two (NGC 4314 and NGC 4636) show X-ray luminosities below the expected value where the torus might disappear ($\log(L_X) < 39.1$ and $\log(L_X) < 39.0$, respectively). Although it is out of the scope of this paper to understand the explanation for the simultaneous occurrence of Compton-thickness and the lack of torus for these three objects, these are not many cases. Furthermore, among our sample, NGC 4321 does not show the multiwavelength signatures of an AGN according to González-Martín et al. (2009a). Thus, 12 of these 14 LLAGNs (excluding NGC 4321 and NGC 4589) are good candidates for the disappearance of the torus.

If the obscuring torus is a smooth continuation of the BLR, i.e., the BLR and torus are the inner and outer bounds of a single cloud distribution (Risaliti et al. 2002; Suganuma et al. 2006; Hönig et al. 2013), the smooth disappearance of the dusty torus might be linked to changes in the structure of the BLR and accretion disk (Elitzur & Shlosman 2006; Elitzur & Ho 2009). Several authors support the disappearance of the torus (e.g., Maoz et al. 2005; Müller-Sánchez et al. 2013) and the BLR according to AGN luminosity (Cao 2010; Elitzur et al. 2014). Recently, Ramos Almeida et al. (2016) showed that the BLR was present for a large portion of their AGNs through polarized emission. However, none of the sources presented in their analysis have bolometric luminosities consistent with the disappearance of the BLR (Elitzur & Ho 2009). Hernández-García et al. (2016) recently showed UV variability in the spatially unresolved nuclear emission of LINERs, consistent with the idea that the torus is no longer obstructing the view of the accretion disk, in contrast with type-2 Seyferts, where no UV point-like source is found for them. Furthermore, absorption variations are not seen in most LINERs, while it appears to be more common in type-2 Seyferts (with higher average luminosities than LINERs; Hernández-García et al. 2016). This is interpreted as a lack of gas clouds close enough to the AGN (i.e., the BLR) to produce eclipses responsible for these absorption variations.

All together, these results show intrinsic differences of LLAGNs compared to more luminous AGNs. Further studies

on the candidates where the torus might disappear, and perhaps those belonging to the group that is close to disappearance (i.e., Group 2, $C_{\rm torus} \sim 20\%$), need to be conducted to verify if the torus is actually disappearing at those LLAGNs.

7. Conclusions

We have studied the torus contribution to the mid-infrared *Spitzer*/IRS spectra of a sample of LINERs and Seyferts, with bolometric luminosities ranging more than six orders of magnitude and used the code DeblendIRS (HC15) to decontaminate the torus emission from the stellar and ISM contributions. We then compared the torus contribution with the bolometric luminosity of the sources. We used the AP method, finding five groups defined by the torus contribution and the AGN bolometric luminosity. These groups have been studied to understand the main differences among them. The main results are:

1. Below a threshold luminosity ($L_{\rm bol} \sim 10^{41}$ erg s^{-1}), we find a negligible torus contribution. This limit is fully consistent with the latest predictions for the disappearance of the torus (Elitzur 2012).
2. The average spectrum of the AP groups with the lowest torus contributions cannot be reproduced by the clumpy torus, even when other contributors are removed from the spectra.
3. Clumpy torus models fitted to the AP groups show that the outer radius of the torus decreases as long as the torus contribution (and $L_{\rm bol}$) decreases. We also found tentative dependencies on the half opening angle of the torus, the height of the torus, and the radial profile of the cloud distribution.
4. We have found a different molecular gas content for those groups with the lowest torus contributions. The S(1), S(2), and S(3) transitions of the H_2 molecular line are only seen in the groups with the lowest torus contributions while S(5) and S(6) are spread among all groups. This might also indicate that the gas content is also changing at the lowest luminosities.

O.G.M. thanks Daniel Asmus for his suggestions that have improved this manuscript significantly. This scientific publication is based on observations made with the Gran Telescopio CANARIAS (GTC), installed at the Spanish Observatorio del Roque de los Muchachos of the Instituto de Astrofísica de Canarias on the island of La Palma. This research has been supported by the UNAM PAPIIT grant (IA100516 PAPIIT/UNAM, 108716 PAPIIT/UNAM), CONACyT grant (CB-2011-01-167291), the Spanish Ministry of Economy and Competitiveness (MINECO, project refs. AYA 2010-15169, AYA2012-31277, AYA 2012-39168-C03-01, AYA2013-42227-P, AYA2015-70815-ERC, AYA2015-64346-C2-1-P, and AYA2016-76682-C3-1-P AEI/FEDER) and by La Junta de Andalucía (TIC 114). M.M.-P. acknowledges support by the UNAM Postdoctoral fellowship programme and C.R.A acknowledges the Ramón y Cajal Program of the Spanish Ministry of Economy and Competitiveness through project RyC-2014-15779. L.H.G. acknowledges ASI/INAF agreement number 2013-023-R1.

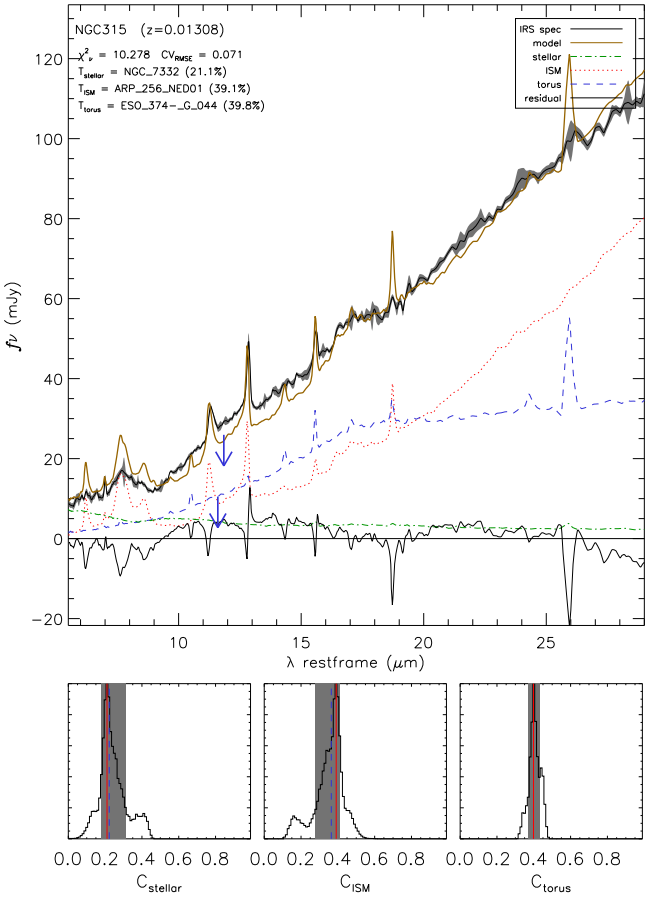

Figure 10. Plots of the spectral decomposition of the *Spitzer*/IRS spectra, as reported by Hernán-Caballero et al. (2015). Note that blue arrows are upper limits derived from the 2–10 keV X-ray luminosity and blue bars are constraints from ground-based high spatial resolution images (see text). The small panels show the posterior distributions for contributions to the 5–15 μm of the stellar, ISM, and torus components.

(The complete figure set (108 images) is available.)

Appendix
Catalog of Spectral Decompositions

Figure 10 shows the plots of the spectral decomposition of the *Spitzer*/IRS spectra, as reported by Hernán-Caballero et al. (2015).

References

Alonso-Herrero, A., Colina, L., Packham, C., et al. 2006, ApJL, 652, L83
Alonso-Herrero, A., Esquej, P., Roche, P. F., et al. 2016, MNRAS, 455, 563
Alonso-Herrero, A., Ramos Almeida, C., Mason, R., et al. 2011, ApJ, 736, 82
Antonucci, R. 1993, ARA&A, 31, 473
Arshakian, T. G. 2005, A&A, 436, 817
Asensio Ramos, A., & Ramos Almeida, C. 2009, ApJ, 696, 2075
Asmus, D., Gandhi, P., Hönig, S. F., Smette, A., & Duschl, W. J. 2015, MNRAS, 454, 766
Asmus, D., Gandhi, P., Smette, A., Hönig, S. F., & Duschl, W. J. 2011, A&A, 536, A36
Asmus, D., Hönig, S. F., & Gandhi, P. 2016, ApJ, 822, 109
Asmus, D., Hönig, S. F., Gandhi, P., Smette, A., & Duschl, W. J. 2014, MNRAS, 439, 1648
Barvainis, R. 1987, ApJ, 320, 537
Bentz, M. C., & Katz, S. 2015, PASP, 127, 67
Brandl, B. R., Bernard-Salas, J., Spoon, H. W. W., et al. 2006, ApJ, 653, 1129

Burtscher, L., Meisenheimer, K., Tristram, K. R. W., et al. 2013, A&A, 558, A149
Cameron, D. T., McHardy, I., Dwelly, T., et al. 2012, MNRAS, 422, 902
Cao, X. 2010, ApJ, 724, 855
Carrillo, R., Masegosa, J., Dultzin-Hacyan, D., & Ordoñez, R. 1999, RMxAA, 35, 187
Cid Fernandes, R., González Delgado, R. M., Schmitt, H., et al. 2004, ApJ, 605, 105
Díaz-Santos, T., Alonso-Herrero, A., Colina, L., et al. 2010, ApJ, 711, 328
Elitzur, M. 2012, ApJL, 747, L33
Elitzur, M., & Ho, L. C. 2009, ApJL, 701, L91
Elitzur, M., Ho, L. C., & Trump, J. R. 2014, MNRAS, 438, 3340
Elitzur, M., & Netzer, H. 2016, MNRAS, 459, 585
Elitzur, M., & Shlosman, I. 2006, ApJL, 648, L101
Emmering, R. T., Blandford, R. D., & Shlosman, I. 1992, ApJ, 385, 460
Frey, B. J., & Dueck, D. 2007, Sci, 315, 972
Gandhi, P., Horst, H., Smette, A., et al. 2009, A&A, 502, 457
García-Bernete, I., Ramos Almeida, C., Acosta-Pulido, J. A., et al. 2016, MNRAS, 463, 3531
González Delgado, R. M., Cid Fernandes, R., Pérez, E., et al. 2004, ApJ, 605, 127
González Delgado, R. M., Pérez, E., Cid Fernandes, R., & Schmitt, H. 2008, AJ, 135, 747
González-Martín, O., Díaz-González, D., Acosta-Pulido, J. A., et al. 2014, A&A, 567, A92
González-Martín, O., Hernández-García, L., Masegosa, J., et al. 2016, A&A, 587, A1
González-Martín, O., Masegosa, J., Márquez, I., et al. 2015, A&A, 578, A74
González-Martín, O., Masegosa, J., Márquez, I., & Guainazzi, M. 2009b, ApJ, 704, 1570
González-Martín, O., Masegosa, J., Márquez, I., Guainazzi, M., & Jiménez-Bailón, E. 2009a, A&A, 506, 1107
González-Martín, O., Rodríguez-Espinosa, J. M., Díaz-Santos, T., et al. 2013, A&A, 553, A35
González-Martín, O., & Vaughan, S. 2012, A&A, 544, A80
Gopal-Krishna, Kulkarni, V. K., & Wiita, P. J. 1996, ApJL, 463, L1
Goulding, A. D., Alexander, D. M., Bauer, F. E., et al. 2012, ApJ, 755, 5
Grier, C. J., Mathur, S., Ghosh, H., & Ferrarese, L. 2011, ApJ, 731, 60
Hatziminaoglou, E., Hernán-Caballero, A., Feltre, A., & Piñol Ferrer, N. 2015, ApJ, 803, 110
Heckman, T. M. 1980, A&A, 87, 152
Hernán-Caballero, A., Alonso-Herrero, A., Hatziminaoglou, E., et al. 2015, ApJ, 803, 109
Hernández-García, L., González-Martín, O., Masegosa, J., & Márquez, I. 2014, A&A, 569, A26
Hernández-García, L., Masegosa, J., González-Martín, O., & Márquez, I. 2015, A&A, 579, A90
Hernández-García, L., Masegosa, J., González-Martín, O., Márquez, I., & Perea, J. 2016, ApJ, 824, 7
Ho, L. C. 2008, ARA&A, 46, 475
Ho, L. C. 2009, ApJ, 699, 626
Ho, L. C., Filippenko, A. V., & Sargent, W. L. W. 2003, ApJ, 583, 159
Ho, L. C., Filippenko, A. V., Sargent, W. L. W., & Peng, C. Y. 1997, ApJS, 112, 391
Hönig, S. F., & Beckert, T. 2007, MNRAS, 380, 1172
Hönig, S. F., Kishimoto, M., Tristram, K. R. W., et al. 2013, ApJ, 771, 87
Horst, H., Gandhi, P., Smette, A., & Duschl, W. J. 2008, A&A, 479, 389
Horst, H., Smette, A., Gandhi, P., & Duschl, W. J. 2006, A&A, 457, L17
Kennicutt, R. C., Jr., Armus, L., Bendo, G., et al. 2003, PASP, 115, 928
Krabbe, A., Böker, T., & Maiolino, R. 2001, ApJ, 557, 626
Krolik, J. H., & Begelman, M. C. 1988, ApJ, 329, 702
Krongold, Y., Dultzin-Hacyan, D., Marziani, P., & de Diego, J. A. 2003, RMxAA, 39, 225
Lawrence, A. 1991, MNRAS, 252, 586
Lebouteiller, V., Barry, D. J., Spoon, H. W. W., et al. 2011, ApJS, 196, 8
López-Gonzaga, N., Burtscher, L., Tristram, K. R. W., Meisenheimer, K., & Schartmann, M. 2016, A&A, 591, A47
Lutz, D., Maiolino, R., Spoon, H. W. W., & Moorwood, A. F. M. 2004, A&A, 418, 465
Maoz, D., Nagar, N. M., Falcke, H., & Wilson, A. S. 2005, ApJ, 625, 699
Marconi, A., Risaliti, G., Gilli, R., et al. 2004, MNRAS, 351, 169
Masegosa, J., Márquez, I., González-Martín, O., et al. 2013, RMxAC, 42, 51
Mason, R. E., Lopez-Rodriguez, E., Packham, C., et al. 2012, AJ, 144, 11
Mason, R. E., Ramos Almeida, C., Levenson, N. A., Nemmen, R., & Alonso-Herrero, A. 2013, ApJ, 777, 164
Mateos, S., Carrera, F. J., Alonso-Herrero, A., et al. 2016, ApJ, 819, 166
Mayo, J. H., & Lawrence, A. 2013, MNRAS, 434, 1593
McKernan, B., Ford, K. E. S., & Reynolds, C. S. 2010, MNRAS, 407, 2399
Mendoza-Castrejón, S., Dultzin, D., Krongold, Y., González, J. J., & Elitzur, M. 2015, MNRAS, 447, 2437
Mor, R., & Netzer, H. 2012, MNRAS, 420, 526
Mor, R., Netzer, H., & Elitzur, M. 2009, ApJ, 705, 298
Müller-Sánchez, F., Prieto, M. A., Mezcua, M., et al. 2013, ApJL, 763, L1
Nenkova, M., Sirocky, M. M., Ivezić, Ž, & Elitzur, M. 2008, ApJ, 685, 147
Nenkova, M., Sirocky, M. M., Nikutta, R., Ivezić, Ž, & Elitzur, M. 2008, ApJ, 685, 160
Netzer, H. 2015, ARA&A, 53, 365
Nicastro, F. 2000, ApJL, 530, L65
Panuzzo, P., Rampazzo, R., Bressan, A., et al. 2011, A&A, 528, A10
Ramos Almeida, C., Levenson, N. A., Alonso-Herrero, A., et al. 2011, ApJ, 731, 92
Ramos Almeida, C., Levenson, N. A., Rodríguez Espinosa, J. M., et al. 2009, ApJ, 702, 1127
Ramos Almeida, C., Martínez Gonzalez, M. J., Asensio Ramos, A., et al. 2016, MNRAS, 461, 1387
Ramos Almeida, C., Pérez García, A. M., Acosta-Pulido, J. A., & Rodríguez Espinosa, J. M. 2007, AJ, 134, 2006
Ranalli, P., Comastri, A., & Setti, G. 2003, A&A, 399, 39
Ricci, C., Walter, R., Courvoisier, T. J.-L., & Paltani, S. 2011, A&A, 532, A102
Risaliti, G., Elvis, M., & Nicastro, F. 2002, ApJ, 571, 234
Roussel, H., Helou, G., Hollenbach, D. J., et al. 2007, ApJ, 669, 959
Sarzi, M., Rix, H.-W., Shields, J. C., et al. 2005, ApJ, 628, 169
Shi, Y., Rieke, G. H., Hines, D. C., et al. 2006, ApJ, 653, 127
Simpson, C. 2003, NewAR, 47, 211
Simpson, C. 2005, MNRAS, 360, 565
Sirocky, M. M., Levenson, N. A., Elitzur, M., Spoon, H. W. W., & Armus, L. 2008, ApJ, 678, 729
Sturm, E., Rupke, D., Contursi, A., et al. 2006, ApJL, 653, L13
Suganuma, M., Yoshii, Y., Kobayashi, Y., et al. 2006, ApJ, 639, 46
Urry, C. M., & Padovani, P. 1995, PASP, 107, 803
Véron-Cetty, M.-P., & Véron, P. 2010, A&A, 518, A10
Wada, K. 2012, ApJ, 758, 66
Willott, C. J., Rawlings, S., Blundell, K. M., & Lacy, M. 2000, MNRAS, 316, 449
Woo, J.-H., & Urry, C. M. 2002, ApJ, 579, 530
Zoghbi, A., Cackett, E. M., Reynolds, C., et al. 2014, ApJ, 789, 56